2022-10-07

The influence of creeping slope failure on turbidity current behaviour

Ayckbourne, AJM

10.1111/sed.13049
Sedimentology
Wiley

Ayckbourne Ashley Jack Manfred (Orcid ID: 0000-0002-5857-2090)
Jerrett Rhodri (Orcid ID: 0000-0002-1412-3808)
Poyatos-Moré Miquel (Orcid ID: 0000-0001-7813-8868)

The influence of creeping slope failure on turbidity current behaviour

Ashley J. M. Ayckbourne[1]*, Rhodri M. Jerrett[1], Miquel Poyatos-Moré[2], Matthew P. Watkinson[3], Ian A. Kane[1], Kevin G. Taylor[1]

[1]*School of Earth and Environmental Sciences, University of Manchester, Manchester M13 9PL, UK*

[2]*Departament de Geologia, Universitat Autònoma de Barcelona, 08193 Bellaterra, Spain*

[3]*School of Geography, Earth and Environmental Sciences, University of Plymouth, Drake Circus, Plymouth, Devon PL4 8AA, UK*

** ashley.ayckbourne@manchester.ac.uk*

Associate Editor – Jaco Baas

Short Title – Controls of creeping MTDs on turbidity currents

ABSTRACT

Erosional scars, slumps, slides and debrites (mass-transport deposits) on submarine slopes form relief that influences turbidity current behaviour. However, the interaction of mass-transport deposit emplacement kinematics (i.e. rapid emplacement *versus* creep), the morphology of the evolving seafloor topography, and subsequent flow types is complicated. This study describes two outcrop examples of deep-water, predominantly turbiditic, deposits overlying mass-transport deposits, from the Eocene slope succession of the Aínsa Basin (Spanish Pyrenees). In both examples, the mass-transport deposit substrate continued to creep contemporaneously with turbidity current deposition and bypass. In the first case study, structures in the mass-transport deposits are extensional and oriented parallel to flow. In the second, structures are compressional and oriented perpendicular to flow. Mudstones dominate the slope succession, but deposits overlying mass-transport deposits form sandstone-prone accumulations. Lateral confinement by flow-parallel extensional faults enhanced channel-formation. Channel incision occurred close to the exhumed fault plane on the hangingwall. Incision ceased as the fault gradually locked-up, and channels avulsed to the hangingwall of a newly

This article has been accepted for publication and undergone full peer review but has not been through the copyediting, typesetting, pagination and proofreading process which may lead to differences between this version and the Version of Record. Please cite this article as doi: 10.1111/sed.13049

active normal fault, while the abandoned channel was filled by a thinning and fining-upward succession. Barriers formed where the long axes of compressional anticlines developed in mass-transport deposits formed perpendicular to flow. Here, turbidites filled the bathymetric lows in the axes of synclines. Continued tightening of synclinal depocentres led to repeated stoss side trapping and up-slope accretion of coarse-grained sediment accumulation. This generated thickening and coarsening-up, followed by thinning and fining-upward successions, tracking the decreasing, then increasing flow bypass associated with topographic expression on the mass-transport deposit. This study shows how post-emplacement creep, and orientation of topographic features on mass-transport deposits, influence the routing and deposition of contemporaneous turbidity currents and illustrates examples of facies successions that could be misinterpreted as the product of other autogenic submarine slope processes, such as lateral migration of sinuous channels, or compensational lobe stacking.

Keywords: Aínsa Basin, creep, Eocene, mass-transport deposit, slope failure, turbidites, turbidity current

INTRODUCTION

Submarine slopes are often dominated by erosive processes, mass-wasting and gravity flows, which form the canyons and channels that transfer sediment to the basin floor (Ross *et al.*, 1994, 1995; Talling *et al.*, 2007; Stevenson *et al.*, 2015; Shanmugam, 2019). However, large volumes of sediment are also retained on the slope, either when slopes are below the graded profile (e.g. Prather, 2000, 2003, when trapped by intra-slope bathymetric obstacles (Spychala *et al.*, 2015), or when fines accrete in off-axis zones (Poyatos-Moré *et al.*, 2016; Boulesteix *et al.*, 2022). Mechanisms of intra-slope depocentre formation are diverse, and include mud and salt diapirism, tectonic extension and compression, (e.g. Prather, 2000, 2003; Helland-Hansen & Hampson, 2009; Ryan *et al.*, 2009; Prather *et al.*, 2017; Nyberg *et al.*, 2018) and gravity-driven slope failures (e.g. Armitage *et al.*, 2009; Kneller *et al.*, 2016; Ward *et al.*, 2018; Bull *et al.*, 2020; Tek *et al.*, 2020; Martínez-Doñate *et al.*, 2021). The latter generate erosional scars, and deposit slumps, slides and debrites, collectively termed mass-transport deposits (MTDs) (Bull *et al.*, 2009; Sammartini *et al.*, 2019; Shanmugam, 2019). The

control that topography generated by these processes exerts on turbidity current erosion, deflection, bypass and deposition is increasingly well studied in outcrop, and in physical and numerical models. Generally, lateral confinement is attributed to flow acceleration, bypass and erosion (Kane *et al.*, 2009; Hodgson *et al.*, 2016; Soutter *et al.*, 2021), while frontal confinement drives rapid flow deceleration and accumulation of thick sand-prone packages up-flow of the obstructing topography (Bersezio *et al.*, 2005; Stevenson & Peakall, 2010; Soutter *et al.*, 2021; Tek *et al.*, 2022).

Slope failures reshape the topography of submarine slopes and can generate significant seabed relief at the evacuation zone and above and around the resulting MTDs. Slope failures involve the down-slope movement of substrate material over a basal shear surface (Fig. 1). There is a growing literature on the kinematic base to MTDs and substrate deformation and entrainment (e.g. Butler & McCaffrey, 2010; Butler & Paton, 2010; Dalton *et al.*, 2017; Braathen *et al.*, 2018; Carey *et al.*, 2019), but considerably less on the kinematic/dynamic nature of the top surface (e.g. Armitage *et al.*, 2009; Martínez-Doñate *et al.*, 2021). Kinematically, their resulting MTDs can be subdivided into: (i) an up-slope extensional headwall domain characterized by a normal sense of movement on the basal shear surface, with or without associated synthetic and antithetic normal faults in the hangingwall; (ii) an intermediate translational domain characterized by (a zone of) bedding-parallel shear at the basal slide surface, transcurrent shear at the lateral margins, and mixed extensional and contractional deformation of the overriding material; and (iii) a down-slope contractional toe domain characterized by thrusting at the basal shear surface, with or without the formation of downslope verging folds and thrust-duplex structures in the hangingwall (Lewis, 1971; Bull *et al.*, 2009).

Down-slope translation of material during failure results in the exhumation of the basal shear surface in the headwall domain, and formation of evacuation scars (Fig. 1). These bathymetric lows are often arcuate in plan view and concave-up in cross-section, reflecting the listric nature of the extensional faulting (e.g. Bull *et al.*, 2009; Kneller *et al.*, 2016; Sammartini *et al.*, 2019; Shanmugam, 2019; Nwoko *et al.*, 2020). Conversely, in frontally emergent mass-transport complexes (MTCs) (e.g. Frey-Martínez *et al.*, 2006), a bathymetric high is generated at the toe domain of the MTD, where transported material accumulates and overspills the frontal ramp, beyond which the MTD

disaggregates forming runout and a debris field. On top of the MTD, relief is generated in the headwall domain where normal fault scarps are exposed at the seafloor, with hangingwall half-grabens forming localized depocentres and/or conduits, which deepen towards the fault. In the toe domain, uplifted hangingwalls of thrusts, as well as folds, can generate bathymetric topographic highs and depocentres on top of the MTD. Hummocky or blocky relief can also be generated on top of the MTD due to megaclasts and pressure ridges or beyond the frontal ramp by outrunner blocks (Bull *et al.*, 2009; Ogata *et al.*, 2012; Hodgson *et al.*, 2018; Ward *et al.*, 2018). Finally, the emplacement of MTDs in existing confining elements such as channels and canyons can result in partial or complete obstruction to the conduit resulting in up-dip accumulation of sediment (Ortiz-Karpf *et al.*, 2015, 2017, 2018; Brooks *et al.*, 2017; Tek *et al.*, 2020). Existing models for the processes by which MTDs generate sediment conduits and subtle confining depocentres (sometimes called 'ponds') which generate accommodation space, often depict this topography as being generated quasi-instantaneously, and subsequently passively infilled and onlapped by later turbidity currents, often by fill-and-spill in the form of prograding intra-slope lobes (e.g. Prather *et al.*, 1998; Sinclair & Tomasso, 2002; Spychala *et al.*, 2015; Brooks *et al.*, 2018). However, some outcrop and seismic studies (e.g. Armitage *et al.*, 2009; Butler & McCaffrey, 2010; Odonne *et al.*, 2011; Kneller *et al.*, 2016; Braathen *et al.*, 2018; Tek *et al.*, 2020) and physical modelling work (e.g. Carey *et al.*, 2019) suggest that the base and top of MTDs can be emplaced in multiple episodes, or via protracted periods of creep during or long after their emplacement, and that conduits can develop via migration of knickpoints above the evolving MTC surface (Tek *et al.*, 2021; Allen *et al.*, 2022).

Using outcrops of an exhumed slope succession from the Eocene of the Aínsa Basin (Spanish Pyrenees), this study aims to: (i) characterize the kinematics (extension *versus* contraction, creep *versus* rapid emplacement) of exhumed MTDs; (ii) characterize the vertical assemblage of deposits on the MTDs; and (iii) develop a model that relates the mode and location of MTD emplacement and the orientation of confining structures on processes of sedimentation, erosion and bypass in the turbidity currents that interact with that topography.

GEOLOGICAL SETTING

The Pyrenees formed from Late Cretaceous to Miocene times in response to the convergence of the Iberian and Eurasian continental plates (Srivastava & Roest, 1991; Muñoz, 2002; Rosenbaum *et al.*, 2002). Two separated foreland basins formed to the north and south of the orogen (Beaumont *et al.*, 2000). The southern foreland was segmented into a series of east–west axially elongated, interconnected piggy-back basins by a set of southerly propagating thrust systems (Fig. 2B). This study focuses on the Early Eocene (Ypresian) slope succession of the Aínsa Basin, which marks the transition from fluvio-deltaic and shallow-marine depositional environments to the east in the Tremp-Graus Basin, to basin floor sedimentation in the Jaca Basin to the west (Nijman, 1998; Payros *et al.*, 2009; Chanvry *et al.*, 2018).

The Eocene slope and basin-floor succession of the Aínsa and Jaca basins is collectively named the Hecho Group (Mutti *et al.*, 1972). However, there are inconsistencies in its chronostratigraphic and lithostratigraphic subdivisions (Mutti *et al.*, 1985; Muñoz, 2002; Remacha *et al.*, 2003; Pickering & Bayliss, 2009; Muñoz *et al.*, 2013; Heard *et al.*, 2014; Cantalejo & Pickering, 2015; Scotchman *et al.*, 2015; Castelltort *et al.*, 2017). Here, the scheme proposed by Clark *et al.* (2017) is followed, wherein seven distinct sand-rich slope channel 'systems' are recognized. From oldest to youngest these are: Fosado and Arro, respectively (Fig. 2D and E) followed by Gerbe, Banaston, Aínsa, Morillo and Guaso (above the vertical extent of Fig. 2D and E) (Burbank *et al.*, 1992; Payros *et al.*, 2009; Poyatos-Moré, 2014; Scotchman *et al.*, 2015; Castelltort *et al.*, 2017; Chanvry *et al.*, 2018), of which the Fosado system is the focus of this study.

METHODS AND DATASET

Two well-exposed MTDs overlain by prominent sand-bodies occur within the slope deposits approximately 10 km east of the town of Aínsa. These are the Barranco de Fosado Section which exposes a portion of the Fosado Channel deposits *sensu* (Mutti, 1977) and (Clark *et al.*, 2017), and another, here named the Samper Ridge Section. Their location and stratigraphic context are illustrated in Fig. 3. The Barranco de Fosado Section is well-exposed for 100 m along the banks of the Barranco (ephemeral stream) de Fosado (42°25'50" N, 0°15'34" E; Fig. 3) and the Samper Ridge Section forms a 600 m long ridge of continuous exposure 0.5 km south of the village of Samper (42°25'19" N,

0°17'06" E; Fig. 3). Geological mapping in this region shows the regional palaeoslope dipped consistently to the north-west for a sustained period in the Cuisian and Lutetian (Millington & Clark, 1995; Castelltort *et al.*, 2017; Tek *et al.*, 2020). At the Barranco de Fosado Section, the palaeoslope was locally dipping towards the south-west, and slope failure structures were dominated by extension, generating fault scarps oriented parallel to regional palaeoflow (Fig. 3). In the Samper Ridge Section, kinematic indicators of deformation conform to the regional north-west-dipping palaeoslope, and are characterized by both extension and compression. Here, topography generated by slope failure is oriented perpendicular to the regional palaeoflow (Fig. 3). Therefore, the sandbodies at the two sites provide a good opportunity to examine flow processes (i.e. erosion, bypass, deflection and deposition) over topographic features oriented parallel and perpendicular to turbidity current direction.

Detailed (1:50 scale) sedimentary logs were collected at both localities (22 in total) with corresponding GPS coordinates, documenting details of the range of sedimentary facies, their thicknesses and correlatable beds/packages. These logs were used to produce structurally restored two-dimensional architectural panels, which were further informed by three-dimensional outcrop models generated from uncrewed aerial vehicle (UAV) photography produced on photogrammetry software (Agisoft Photoscan). Palaeoflow readings were recorded from flutes, grooves and ripples, and slope failure directions were interpreted from soft sediment deformation indicators such as slump-fold vergence and thrust vergence, and normal fault-plane dip directions.

FACIES ASSOCIATIONS

Six lithofacies are defined (Lf1 to Lf6, Table 1), based on grain size, nature of contacts, grading, sedimentary structures and average bed thickness. These lithofacies stack to form five different facies associations (FA1 to FA5, Fig. 4). The transition between these facies associations can be vertically and laterally gradational across several metres.

Facies Association 1 – Mudstones

Description – This is the most volumetrically prevalent type of deposit in the study area and forms the most laterally continuous successions in the stratigraphy. It is characterized by a prevalence of thin

bedded mudstones (Lf2 and Lf3, Table 1, Fig. 4), occasionally containing isolated thin-bedded ripple laminated sandstones (Lf4) and rarely interbedded with structureless mudstones (Lf1).

Interpretation – Thin-bedded normally-graded Lf2 mudstones and thin-bedded Lf4 sandstones are interpreted as the deposits of low-concentration turbidity currents (Mutti, 1977, 1992; Jobe *et al.*, 2012; Talling *et al.*, 2012) and are likely the result of sediment collapse on the slope, in the feeder canyon, or on the shelf (for example, mouth-bar collapse; Hughes Clarke, 2016). It is possible that flows that delivered these sediments were low-concentration and mud-laden, or that these deposits resulted from the dilute tails of flows where coarser sediments in the head of the flow bypassed (e.g. Stevenson *et al.*, 2015). This interpretation is supported by thin lags at the base of mudstone beds composed of fine to very fine-grained sandstones. The low prevalence of hemipelagites (Lf1) suggests that most suspension-settled sediment was reworked into subsequent turbidity currents. The normally and inversely graded mudstone (Lf3) deposits are interpreted as hyperpycnites, where grading and grain size is controlled by fluctuations in the sediment flux delivered by direct river influence via the deltaic point source (Mulder *et al.*, 2003; Bhattacharya & MacEachern, 2009; Zavala & Pan, 2018). However, Mutti, (2019) has recently suggested that these deposits throughout the Hecho Group could also be the result of sediment-laden collapse of hypopycnal plumes.

Facies Association 2 - Heterolithic thin beds

Description – This facies association is characterized by an increased prevalence of sandstone beds and a declining prevalence of mudstones, with respect to the mudstone facies association (FA1). It comprises higher frequency interbedding of mudstones (Lf1, Lf2 and Lf3), and thin-bedded rippled sandstones (Lf4) that are occasionally scoured at the base. Individual sandstone beds frequently pinch and swell and often form isolated beds with concave-up and slightly scoured bases. Whole packages of this facies association are frequently laterally discontinuous and pinch out against underlying deposits, however, the bases of these successions are rarely erosional.

Interpretation – As in the Mudstones association (FA1), thin, normally-graded mudstones (Lf2), normal/inverse graded laminated mudstones (Lf3) and thin, normally-graded sandstone beds (Lf4) are interpreted as deposits of low-concentration sediment gravity flows. Where scouring is identified at

the base of individual beds, it is interpreted that the coarser high-concentration part of flows bypassed downstream, leaving behind the deposits derived from the finer-grained tails (Stevenson *et al.*, 2015). Alternatively, where scoured bases of individual beds are ornamented by flutes and grooves they can also represent the infill of an erosion surface left by preceding flows (Kane *et al.*, 2009; Peakall *et al.*, 2020). Where bases of successions comprise this facies association, they vary laterally in thickness, with concave-up bases and exhibit minimal erosion at the base; this is interpreted as the infilling of topography generated by soft-sediment deformation of the substrate material.

Facies Association 3 - Amalgamated thin-bedded sandstones

Description – This facies association is dominated by sandstones, and mudstones are absent or subordinate. Sole structures (flute, groove and gutter casts) are common at the base of beds as well as minor erosive surfaces (>1 m deep) and frequent amalgamation between sandstone beds. It is composed of thin-bedded rippled sandstones (Lf4), normally graded (Lf5a) and structureless (Lf5b) sandstones (Table 1; Fig. 4) and from packages ranging from approximately 0.3 to 2.0 m. Infrequently, thin deposits (up to 50 cm thick) of mudstones (Lf1, Lf2 and Lf3) can be interbedded between sandstone beds. Sandstone beds that are erosive at their base, scoured into underlying mudstones and/or sandstone beds and formed amalgamation surfaces that can be marked by horizons of muddy rip-up clasts and/or mudstone flame structures.

Interpretation – As in FA1, thin, structured and normally-graded Lf4 sandstone beds are interpreted as the deposits of low-concentration sediment gravity flows. Unstructured (yet normally graded) Lf5a sandstone beds represent deposition from high-concentration turbidity currents with high aggradation rates, preventing the formation of internal structures or hindrance and *en masse* deposition of liquified debris flows (such as traction carpets at the base of flows) (Kneller & Branney, 1995a; Sumner *et al.*, 2008; Talling *et al.*, 2012). Amalgamated, thin bedded, and structured sandstone successions have been interpreted as off-axis lobe deposits due to rapid deceleration of turbidity currents (Mutti, 1977; Prélat *et al.*, 2009; Marini *et al.*, 2015; Kane *et al.*, 2017; Bell *et al.*, 2018); however, here it is proposed that these successions can also form in intra-slope environments, where flow deceleration can occur as turbidity currents interact with a complex seafloor topography.

Facies Association 4 - Thick-bedded sandstones

Description – Only normally-graded (Lf5a) and structureless (Lf5b) sandstone beds make up this facies association, with negligible to a complete absence of mudstones (Fig. 4). These beds overlie erosive surfaces that incise from 0.5 m to more than 5,0 m of stratigraphy, or overlie features such as slump structures where topographic relief is greater than metre to decimetre scale. These deposits often comprise multiple amalgamation surfaces that can be recognized by horizons of mudstone rip-up clasts and abrupt changes in grain size. The combined thickness of these sandstone deposits ranges from 1 m to >5 m. The thickest parts of these successions are often massive with dish structures observed, and where they are deposited on top of mudstones and MTD mudstones, the base of the deposits frequently exhibit large load structures and mudstone flames that can intrude up to 0.5 m into the overlying sandstone deposits.

Interpretation – As in FA3, thick, structureless sandstone beds of Lf5a and Lf5b result from rapidly aggrading sediment deposited from decelerating high-concentration turbidity currents. The increased prevalence of amalgamation between beds, and entrainment of mud clasts indicate that the formative flows were high-energy with high tractional forces enabling them to erode and entrain the substrate material from upstream of the locus of deposition (Kneller & Branney, 1995b; Talling *et al.*, 2012; Stevenson *et al.*, 2015). These deposits increase in prevalence towards the axial part of depositional settings, where sediment concentration is highest or where flows are more laterally confined; they have been observed in channel-fill deposits (Wild *et al.*, 2005; Talling *et al.*, 2012) and lobe-axis deposits (Prélat *et al.*, 2009).

Facies Association 5 – Mass-transport deposits

Description – This facies association is defined by remobilized substrate composed of other the facies associations, and comprises coherent, folded and rafted deposits (MTDa), faulted, disaggregated and plastically deformed deposits (MTDb) and of chaotically disaggregated deposits (MTDc) (Table 1; Fig. 4). Individual MTDs are generally >1 m thick and can be sharp or scoured at the base and can occur individually, or stack to form successions up to 30 m thick. These deposits are heterolithic and

varied in composition; MTDa–MTDb can be composed of any sedimentary lithofacies described in Table 1, or be comprised of entire packages of facies associations FA1–FA4. Cohesive and folded deposits of MTDa and partially disaggregated MTDb deposits, are frequently found above MTDc, and are most often composed of heterolithic thin beds (FA2), amalgamated thin beds (FA3) or thick-bedded sandstones (FA4). Chaotic deposits of MTDc are most frequently composed of mudstone deposits (Lf1, Lf2 and Lf3, Table 1) forming a matrix with rare clasts of sandstones (Lf4, Lf5a and Lf5b, Table 1).

Interpretation – Cohesive and folded successions of other facies associations described in MTDa are consistent with elastic and plastic deformation of coherent masses termed slump and slide deposits (Lewis, 1971; Ogata *et al.*, 2012; Shanmugam, 2019). The mudstone dominated, poorly sorted, chaotic, folded and faulted, clast-rich nature of MTDc deposits is interpreted as deriving from gravitational collapse and *en masse* deposition of debris flows generated by down-slope remobilization of substrate material, often termed debrites (Ogata *et al.*, 2012; Talling *et al.*, 2012; Shanmugam, 2019). Deposits that are slumped, faulted and partially disaggregated (MTDb) occupy a mid-ground between slumped deposits (MTDa) and debrites (MTDc) where cohesive slides and slumps failed to fully mobilize as an *en masse* flow.

RESULTS

Barranco de Fosado Section

Exposures of the Fosado Channel sandbody (Fig. 6A) occur approximately 250 m west of the exposure of the tectonically controlled Atiart Thrust (Fig. 3). Palaeoflow readings from flutes and grooves indicate a predominant flow direction towards the north–NNW (Fig. 5C), rather more north-directed than regional observations (Fig. 3). Subordinate flow directed towards the west to south-west is indicated by bed-top ripple data. Kinematic indicators for soft sediment failure indicate that the structures at and near the Barranco de Fosado Section moved down slope towards the west to south-west (Fig. 5C). Therefore, structures generated at this locality are oriented parallel to regional palaeoflow. The exposure (Fig. 5A and 5B) is oriented north-east/south-west, parallel to the direction of local slope failure.

Description – The overall architecture of the section is characterized by a master south-west-dipping fault (F1; Figs 4 and 5), which juxtaposes a wedge of turbidite sandstone facies association deposits (FA2–FA4) and debrites (FA5) against a thick succession of thin-bedded mudstones (FA1) to the north-east (Fig. 6B). The turbidite sandstones and debrites thin and fine towards the south-west away from the master fault (F1). Strata overlying and underlying the sandbody are not well-exposed. Internally, the sandbody can be sub-divided into seven erosively-based, fining-upward and thinning-upward successions (T1–T7; Figs 5B and 6). The basal erosional surfaces cut down up to 5 m into the underlying strata and are commonly overlain by mudstone debrites (FA5), containing up to cobble-sized sandstone clasts, or thick-bedded amalgamated sandstones (FA4) passing upward to finer and more thinly-bedded sandstones and mudstones (FA3 to FA1). Beds tend to thicken and coarsen towards the axis of the basal erosional surfaces (for example, T4 and T5; Fig. 6B), and also tend to thin and fine away towards their onlap against the scour margin. Lower order erosion surfaces, occurring at the bases of individual beds and amalgamated bed packages erode more deeply in the axis of the erosional scour and become less erosional towards the scour margins (for example, T2 and

T5; Fig. 6B). Palaeocurrent directions within these fining-upward and thinning-upward successions range from WNW/south-west for ripples, and towards the NNW for sole structures (Fig. 6C).

As well as the master fault (F1), four smaller, south-west-dipping, listric normal faults occur within the Barranco de Fosado Section (F2–F5; Fig. 5). Fining-upward and thinning-upward packages show several systematic stratigraphic relationships with these faults. Firstly, they thicken towards the fault planes in their hangingwalls, and successive beds dip less steeply towards the fault. This relationship is observable at the scale of the whole section, where T1 to T5 thicken towards the master fault (F1; Fig. 5). It also occurs at the scale of individual fining-upward and thinning upward successions, where for example T2 thickens towards fault F2 (Fig. 5). Stratigraphy in the hangingwall of some normal faults also exhibits weak monoclinal to open synclinal geometries about 2 to 3 m wide against the fault plane (for example, faults F4 and F5; Fig. 5) where beds pinch out against the fault and show minor growth towards the synclinal axis (for example, T6 and T7; Fig. 5). By contrast, strata on the footwall side of the faults do not form conjugate anticlines, but instead are generally horizontally bedded. Finally, the erosional bases of fining-upward and thinning-upward packages excavate hangingwall stratigraphy most deeply adjacent to fault planes. This is clear where T5 cuts down more than 5 m of stratigraphy from south-west to north-east towards fault F1 (Fig. 5). This also occurs where the scour at the base of T2 excavates the hangingwall stratigraphy of fault F2; this surface also truncates the F2 fault plane. More subtly, the erosional surface at the base of T3 downsteps above the hangingwall to footwall stratigraphy of faults F2 and F3. The erosional base of T4 also downsteps into the hangingwall above fault F3, which is further reflected in basal scours of individual beds where more small-scale erosion occurs above these hangingwalls (Fig. 5).

Interpretation – Contemporaneous activity on the Atiart Thrust (Fig. 3), cropping out just 250 m to the north-east of the Barranco de Fosado Section may have been responsible for the development of the local palaeoslope. The presence of this palaeoslope is evidenced by the vergence direction of slump folds thrust faults, and the orientation of normal faults towards the south-west to west at this location (Figs 3 and 6). Additionally, the deviation of palaeoflows

towards the north/NNW compared to the usual north-west regional palaeoflow (parallel to the strike of the thrust) suggest that flows may have been funnelled through the syncline in the footwall of the Atiart Thrust (see Fig. 3). Whatever the cause of the local change in palaeoslope, the long-axial orientation of palaeo-bathymetric relief generated by slope failures was parallel to palaeoflow. The >1 m thick chaotic mudstone deposits containing sandstone clasts are interpreted as possible lags left by bypassing flows. Based on the concave-up morphology of erosional scours, and prevalence of erosion and bypass indicators, the erosionally-based fining and thinning-upward successions are interpreted as channel-fills (e.g. Mutti & Normark, 1987; Casciano *et al.*, 2019). Fining and thinning-upward successions occur when flows no longer bypass via the channel or conduit and instead become depositional resulting in the progressive infill and ultimate spill of the scour. Alternatively, thinner and finer deposition could be derived from overbanking flows of a new contemporaneous channel once the observed channel was no longer the main conduit. The thickening of strata towards the footwall of listric normal faults, the deepening of channel scours towards fault planes in the hangingwall and synclinal growth strata in the hangingwall, combined, suggest that the faults, including master fault F1 were active synchronously with deposition at the Barranco de Fosado Section.

The presence of monoclinal or open synclines in the hangingwalls of faults F4 and F5 that pinch towards the fault plane but exhibit growth towards the syncline axis are indicative of faults that were not exposed at the seafloor but active in the near subsurface (blind faults) (e.g. Hodgson & Haughton, 2004). This suggests that no significant bathymetric relief was generated by faults F4 and F5, which explains why finer grained and thinner bedded deposits are found in the hangingwalls of these faults.

The up to 90 degree disparity in palaeoflow from flute casts and grooves at the base of beds (strongly NNW) versus bed-top ripples (ranging WNW to south-west) resulted from the gradual change in flow direction as sediment gravity flows decelerated (Fig. 6C), recording a disparity between head of flows that carry the momentum of their initial flow direction and the tails of flows which are more susceptible to deflection off topography. Grooves and flutes are formed by tractional or turbulent scouring of the sediment substrate by passing the load transported towards the base flows, by either laminar cohesive debris

flows or by turbulent dilute flows, respectively (Peakall *et al.*, 2020), whereas ripples are formed by tractional reworking of grains that have settled from suspension in more dilute flows (Allen, 1982; Lowe, 1982; Jobe *et al.*, 2012; Talling *et al.*, 2012). Features indicative of the bypass-dominated or higher concentration phase of a flow (sole structures) are oriented parallel to the strike of normal faults and are consistent with regional palaeoflow (north-west) throughout the wider study area (Fig. 3), indicating that the axis of erosional flows was approximately perpendicular to local palaeoslope and parallel to the axis of palaeo-bathymetry generated by slope failures (Fig. 6). Ripples formed by the decelerating, low concentration tails of flows show a range of orientations from WNW to south-west (Figs 5 and 6). These lower concentration tails of flows conform to the local west/south-west verging slope failure, suggesting that as the flows decelerated their flow direction increasingly deflected to conform with local westerly palaeoslope derived from the nearby Atiart Thrust to the East.

Cross-cutting relationships between scours, fault planes and bed onlap terminations show that faults did not form or propagate at the same time. As T1 to T5 deposits all exhibit growth towards fault F1, this fault is interpreted as the oldest structure, which was active from at least times T1 to T5 (Fig. 6). Fault F2 was active at the same time as the T2 channel scour formed and early T2 deposits accumulated, as identified from growth in the hangingwall and channel deepening towards the fault plane. The T2 channel scour and early fill is cut by fault F3 without growth in the lower T2 deposits. Growth is identified in the upper T2 strata in the hangingwall of F3; at this time the footwall flank of F2 was eroded and passively overlain by upper T2 strata. F4 and F3 remained active through T3 and T4 where the sites of channelization remained above the half grabens of these two faults although their fault planes were only active beneath the surface with no further propagation of their escarpments. During T5, the locus of channelization returned to the hangingwall of F1. F4 cuts stratigraphy up to T5, with coeval deposition of T6. Finally, fault F5 cuts T6 stratigraphy, during deposition of T7

Samper Ridge Section

The ridge occurs 0.5 km south of the village of Samper, and forms 600 m of near continuous north-east/south-west trending exposure of a prominent sandbody (Fig. 7B). Palaeoflow readings (from flutes, grooves and ripples) indicate that flow direction was to the north-west/NNW. Soft-sediment fold and thrust vergence was also to the NNW (see mean vectors in Fig. 3), therefore structures generated by slope failure formed local bathymetric barriers oriented perpendicular to the flow direction. The exposure, and therefore the panel in Fig. 7, is approximately oriented along the oblique dip of local palaeoslope.

Description – The Samper Ridge Section is divided into upper and lower sandstone packages (Fig. 7). The Lower Sandbody, which was deposited above an up to 6 m thick mudstone debrite (labelled MTD A), is separated from the Upper Sandbody by another 4 m thick mudstone debrite (labelled MTD B). The debrites are not well-exposed, but the limited kinematic data available from slump fold and thrust vergence imply a transport direction towards the north-west (Fig. 3). North/NNW verging thrusts and folds deform both sandstone packages. Thrusts are rooted into the underlying mudstone-dominated debrites (FA5; MTD A and MTD B) where the fault planes dissipate. Towards the south-west, the Upper Sandbody is also characterised by a north-dipping thrust fault, the strata in the hangingwall of this thrust thicken southwards towards the hangingwall anticline and fault plane (F8) (Fig. 7). The sandbodies are segmented laterally into asymmetrical lens-shaped packages of FA1 to FA4 that thin and fine over thrust tips and anticlines and thicken into syncline axes; individual beds up to 1 m thick in the axis of synclines can thin to less than 5 cm at the anticlines. The lenticular sandstone packages vary in thickness from 1.0 to 4.5 m, thicken and coarsen towards the axes of synclines, and thin and fine towards anticlines and thrust crests. Internally, the lens-shaped packages are not erosional at the base, and are characterized by a succession of beds that thicken towards the syncline axes. Older beds are more tightly folded into the syncline axes, and stratigraphy becomes more flat-bedded upward through the succession. The vertical successions commonly thicken and coarsen upward from mudstones and thin-bedded sandstones to thick-bedded sandstone deposits (FA1 and FA2 to FA3/FA4, for example, Log 1 to 4), and then thin and fine upward back to mudstones and thin-bedded sandstones. Scour surfaces are uncommon and restricted to the amalgamated sandstone-prone portions of these successions at the

inflexion from coarsening and thickening-upward to fining-upward and thinning upward in the axes of the synclines. Here, scours are up to 1 m deep concave-up surfaces on to which inclined beds of fine to medium grade sandstone containing up to cobble-sized mudstone rip-up clasts (FA4) downlap, most clearly seen in the thick-bedded coarser-grained portions of logs L6, L7 and L8. The inclined beds dip south-east (up-palaeoslope) and are also erosionally-based. In the Upper Sandbody, deposits have a wedge-shaped geometry, thickening towards the south-west against the F8 fault plane, and increasing the combined thickness from 2.5 m (north-west) to 6 m (south-west).

Interpretation – The systematic thickening of beds towards syncline axes within the lenticular sandstone packages at the Samper Ridge Section indicate that the structures were active at the time of deposition. Bed correlations across F8, as well as the thickening of packages around the hangingwall anticline towards the fault, suggest that this structure was active as a normal fault at the time of deposition and was later inverted by contraction to form a thrust fault. Structures are rooted in the MTDs and verge in the direction of the local palaeoslope which strongly indicates that deformation was controlled by down-slope creep. It is therefore interpreted that after the emplacement of MTD A there was continued shear within the MTD, and at the base of the deposit from which folds and faults were able to propagate, forming bathymetric ridges on the seabed. Faults F5 and F6 propagate through both MTD A and MTD B, which suggests that structures initiated by MTD A remained active long after deposits being buried by MTD B.

In the lens-shaped sandstone packages, the systematic thickening of beds into the syncline axes, and the fact that each bed is less folded into the syncline than the last leads to the conclusion that these sandbodies were not deposited into a deep pre-formed ‘pond’ which was passively filled by the resultant deposits of subsequent flows. Instead, accommodation was generated and filled incrementally by turbidity currents which would otherwise have bypassed. Therefore, the thickness of the resulting package does not reflect the bathymetric relief of the ponds at any given time, because this relief was being incrementally created at the same time that it was being partially filled.

In the upper and lower sandbodies, the coarsening-upward and thickening-upward followed by fining and thinning-upward successions imply an apparent waxing and then waning of flow energy and concentration. This apparent change in energy likely relates to changes in the amount of flow confinement as the topographic expression of barriers generated by growing anticlines increased and then decreased as the topography was filled-up, as a ratio of sedimentation rate to deformation rate. Following the initial virtually instantaneous emplacement of a mudstone-rich debrite, the MTD continued to creep downslope which resulted in predominantly compressional zones and some extension (fault F8), generating relief on the seabed. Initially, relatively subdued topographic relief was infilled by the tails of largely bypassing turbidity currents (FA1 and FA2). Continued movement on the MTD enhanced the amount of local accommodation, and successively thicker and coarser beds were deposited and incorporated in the creeping MTD, as flows that would otherwise bypass down-slope were trapped. As the rate of deformation outpaced sedimentation, more pronounced topography developed to increase the rate of flow deceleration resulting in deposition of thick-bedded and occasionally amalgamated sandstones. Due to the abrupt change in topography some of the flows initially scoured the underlying substrate before rapidly depositing their sediment (FA4). As the rate of creep on the MTD decreased, topographic lows were gradually filled by ponded fill-and-spill processes where progressive flows were increasingly able to bypass as less accommodation remained to trap sediment.

Up-flow dipping amalgamation surfaces and accreting beds overlying an erosive surface occurred in some T3 deposits on the up-flow side of folds and thrust faults (Fig. 9). These up-flow accreting deposits are comparable to those formed by upstream-migrating bedforms, formed when flows undergo abrupt deceleration due to sudden changes in seabed topography (Cartigny *et al.*, 2014; Postma & Cartigny, 2014; Covault *et al.*, 2017; Soutter *et al.*, 2021). This suggests that occasionally structures were able to propagate and generate abrupt topographic change resulting in erosion on and behind the highs, while in most locations no significant bathymetric highs were generated.

DISCUSSION

At both localities, kinematic features within MTDs, and the overlying deposits demonstrate that MTDs can creep as an initiation mechanism (i.e. normal faults at the Fosado Section) or continue to creep after initially rapid emplacement (i.e. debritic deposits at the Samper Section), incorporating the overlying turbiditic deposits into the creeping process. Consequently, it is difficult to separate the MTDs from the overlying deposits, at least to the point where flat-lying fine-grained slope deposition resumed, with little evidence for further movement on the MTD. Processes of long-term creep, and incorporation of stratigraphy into 'deposits' have been recognized in longer-term, larger-scale basin-margin collapse systems, from seismic reflection data (e.g. Rowan *et al.*, 2004; Butler & Paton, 2010; Dalton *et al.*, 2017; Chima *et al.*, 2022), and here, as with Butler & McCaffrey (2010) , a similar, albeit smaller-scale and shorter-term process and deposit for slope MTDs is invoked.

At the Barranco de Fosado Section, a succession of normal faults were formed (Fig. 6) and propagated gradually and coevally with sedimentation, exhuming fault scarps and rotated half-grabens on the seafloor. Consequently, confinement was achieved without the need of significant erosion. However, there is still evidence that some erosion of the substrate and fault scarps happened, by the flows that exploited this morphology. At the Samper Ridge Section, accommodation was generated in low-amplitude synclines (Fig. 7). Here, subtle seafloor lows were generated in subsiding synclines, but readily filled by sand from multiple flows that would otherwise have bypassed the undeformed slope. Continued subtle growth with contemporaneous deposition led to the formation of sandbodies that are much thicker than the vertical extent of the depocentre would have been at any given time during the emplacement of these deposits. These observations contrast with existing models that depict MTDs as rapidly emplaced deposits, over which later deposits onlap and drape (e.g. Armitage *et al.*, 2009; Kneller *et al.*, 2016; Kremer *et al.*, 2018; Ward *et al.*, 2018), even where rapid emplacement occurred by debris flow deposition the subsequent deposit continued to creep long after emplacement (i.e. Samper Ridge Section). Even though MTDs analysed in this study eventually ceased in

their downslope movement, the deposits overlying them clearly evidence a period of a creeping and mobile seafloor that influenced the routing and deposition of later deposits.

Orientation of kinematic features versus turbidity current flow direction

The main differences between the two studied localities is the development of fining and thinning-upward erosionally-based successions at the Barranco de Fosado Section compared to non-erosionally-based thickening and coarsening-upward followed by thinning and fining-upward successions at the Samper Ridge Section (albeit with the development of erosional surfaces within the middle, coarsest part of the deposit). Were these differences caused by the orientation of the confining structures (parallel to flow at the Barranco de Fosado Section, and perpendicular to flow at Samper Ridge Section), or differences in the mode of topography formation on the seafloor (i.e. extension at the Barranco de Fosado Section *versus* predominantly compression at the Samper Ridge Section)?

The behaviour of sediment gravity flows when encountering topographic barriers has been demonstrated to differ according to the orientation of the obstruction relative to the vector of the flow (Brunt *et al.*, 2004; Pohl *et al.*, 2020; Soutter *et al.*, 2021). The orientation of these structures can control flow deflection, reflection, deposition, bypass and deposit morphology (see Fig. 10). At the Barranco de Fosado Section, the initial high-velocity portion of sediment gravity flows travelled approximately parallel to the strike of topography-generating normal faults. Increasing confinement of sediment gravity flows by laterally confining topography has been shown to increase flow velocity, enabling flows to erode and sediment to reach further down-slope (Kneller, 1995; Hodgson *et al.*, 2016).

Channels in the Barranco de Fosado Section were asymmetrical, with steeper channel margins adjacent to the fault plane, and deeper incision towards the fault planes on the hangingwall. These asymmetrical channels confined flows more strongly on one flank. Soutter *et al.* (2021) demonstrate that when only

one flank of a density flow is confined by a barrier the overall velocity can still be enhanced by increasing (or maintaining) the concentration of the flow next to the obstacle. Gradual formation of topography by movement on the faults may have gradually enhanced the erosional power of the flows, leading the formation of more strongly erosional surfaces, until the rate of movement on the fault began to decrease, covering the deepest scour (the basal erosion surface). This erosion surface was then overlain by the deposits of off-axial flows that gradually decreased in their erosive power and capacity to carry sediment while the axial portion of these flows were redirected laterally and trapped by confinement generated by younger structures.

At the Samper Ridge Section, structures were oriented approximately perpendicular to the dominant transport direction, forming frontally confining barriers to passing sediment gravity flows. As these structures grew contemporaneously with sedimentation these barriers drove rapid deposition of sediment on the up-flow side of the barrier. In these deposits, erosion is confined to bed-scale basal scours, which occur within the coarsest, middle part of the deposits. These coarsest packages are also characterized by beds that dip in the up-flow direction that contain large (cobble-sized) mudstone rip-up clasts. These observations are consistent with numerical models and experimental observations for rapid reductions in sediment gravity flow velocity where there are frontal barriers (for example, channel-lobe transition zones or at points of significant change in slope topography) (Postma & Cartigny, 2014; Covault *et al.*, 2017; Brooks *et al.*, 2018; Howlett *et al.*, 2019; Pohl *et al.*, 2020; Soutter *et al.*, 2021).

Model for the influence of creeping MTDs on turbidity currents

Existing studies show that slope gradient and the progressive development of flow confining morphology impact depositional, bypass and erosional thresholds of sediment-laden flows (e.g. Kneller, 1995; Brunt *et al.*, 2004; Armitage *et al.*, 2009; Pohl *et al.*, 2020). For example, (Hodgson *et al.*, 2016)) show that in deep-water channels, the development of levees increases confinement and drives incision. In 'ponded' geometries, Armitage *et al.* (2009) show that successive deepening of a depocentre by foundering of rafted blocks on a muddy MTD results in the trapping of sand partitioned by chaotic morphology.

In this study a mechanism is proposed for the influence of the time-transgressive formation of confining topography by creeping MTDs on depositional and erosional processes and resulting architecture of sediment gravity flow deposits (Fig. 10). Although, as discussed above, the vertical assemblage differs according to the orientation of the axes of structures *versus* flow direction, a generic model can be developed:

Stage 1: Initiation and early creep

The formation of local depocentres and barriers on a creeping kinematic feature (for example, normal faults, folds and thrusts) outpaces the rate of sediment infill, and the accommodation and overall confinement of the depocentres increase. In laterally confined settings, this can result in increased flow concentration and consequently, acceleration of the flows driving localized erosion and bypass, and the generation of conduits and channels (Hodgson *et al.*, 2016; Soutter *et al.*, 2021). In frontally confining structures, generation of topography can prevent sediment bypass and will result in the deposition of increasingly thicker and coarser grained beds. Successions of progressively coarsening and thickening successions have been identified, for example at intraslope basin-scale (tens of metres to kilometres) in the Annot Basin (France) and between mud diapirs of the Gulf of Mexico (Sinclair, 1994; Sinclair & Tomasso, 2002; Brunt *et al.*, 2004; Soutter *et al.*, 2019). Sinclair & Tomasso (2002) propose that such successions are directly controlled by a syn-depositional increase in depocentre confinement. Connectivity between confining depocentres occurs by flows over-spilling between partially confining topography or by conduits forming between depocentres initiated by subtle erosion and knickpoint migration (e.g. Tek *et al.*, 2021; Allen *et al.*, 2022).

Stage 2: Maximum topographic relief

This stage is marked when topographic confinement is at its greatest. This likely happens at the point at which creep first begins to slow as the MTD locks up. In laterally confined settings, conduit/channel deepening by active kinematic processes (for example, deep normal fault half grabens at the Barranco de Fosado Section) and erosion is replaced by net-deposition. This change from net erosion to deposition is likely due to the autogenic recovery of the slope to

its equilibrium profile while bypassing flows switch to a new optimum path (such as where a new fault is generated at the Barranco de Fosado Section). In frontally confined settings the maximum vertical displacement of the depocentre results in the rapid deposition of sediment on the stoss side of the obstruction. The greater palaeo-bathymetric relief results in localized bed-scale scouring due to enhanced turbulence generated in the passing flows by bed roughness.

Stage 3: Late to post-creep

When the infill of slope depocentres outpaces the rate of accommodation generation on the MTD, these bathymetric lows are gradually healed. The processes by which passive topography is infilled has been well-studied and is often referred to as 'fill and spill' (Prather *et al.*, 1998; Booth *et al.*, 2000; Prather, 2003; Brunt *et al.*, 2004); where initially trapped flows deposit quasi-all of their sediment resulting in coarser and thicker deposits but as the depocentre is filled, successive flows bypass more easily, resulting only the finer tails being deposited. Consistent with these studies, post-creep depositional successions are characterized by progressive thinning and fining of beds. However, although sedimentation outpaces creep, the MTDs in these case studies were not yet static, therefore this stage still comprises deposits that exhibit growth geometries towards the axes of the depocentres (Figs 10 and 11).

Comparing vertical stacking patterns on creeping topography to other deep-water deposits

In deep water settings, coarsening and thickening-upward successions on the 1 to 10 m scale are often observed in migrating deep water lobes or lobe elements (e.g. Mutti, 1977; Macdonald *et al.*, 2011), and thinning and fining-upward successions on the 1 to 10 m scale are often seen in channel-fill deposits (e.g. Hubbard *et al.*, 2014; Jobe *et al.*, 2017). Such successions are generally interpreted to represent autogenic processes such as lobe advancement or channel avulsion, or by allogenic processes such as the advancement or retreat of systems as a result of basin-scale changes in accommodation or sediment supply.

These successions are often looked for in subsurface datasets, such as in core or geophysical wireline logs, when attempting to interpret depositional facies, form palaeogeographic models and reconstruct extrinsic controls on sediment architecture. However, in this study erosionally-based, fining and thinning up successions at the Barranco de Fosado Section, although representing a form of conduit or channel-fill, were controlled in terms of their location and geometries by the locus of creeping normal faults on MTDs. The coarsening and thickening up, followed by fining and thinning up successions in the folded depocentres at the Samper Ridge Section, although resembling lobe elements, were formed by the gradual infill of synclines developing contemporaneously with deposition on a creeping MTD. This study shows that there are alternative mechanisms for the formation of often-observed sedimentary architectures in slope settings, which should be taken into account when making predictions about the lateral variability of these deposits. For example, the presence of a conventional lobe implies the presence of a feeding channel and potentially channel fill deposits in the up-flow direction. However, the rugosity of MTD topography means that such predictions should not be made when interpreting turbidity flow deposits on creeping MTDs.

CONCLUSIONS

Two outcrop examples of slope failure deposits comprising structures oriented parallel and perpendicular to palaeoflow were compared in order to study the interaction of sediment gravity flows with dynamic mass-transport deposit (MTD) topography. In this study, all topographic features associated with MTD emplacement in the Fosado System of the Eocene Aínsa Basin exhibit evidence of dynamic creeping topography that coincided with turbidity current activity on the slope.

At the Barranco de Fosado Section, slope failure was predominantly extensional with the strike of normal faults oriented parallel to palaeoflow. Consequently, lateral confinement by the fault escarpments and subsiding half-grabens initiated and enhanced channel formation, with scours incising steeply

and deeply towards fault planes. Channelization was most prevalent on active faults, and when a fault became inactive, that channel avulsed to newly active faults nearby, while the abandoned channel was filled by fining up successions from thick sandstone beds to thin-bedded mudstones.

Slope failure at the Samper Ridge Section was predominantly compressional with the axis of fold and thrust structures oriented perpendicular to the palaeoflow direction generating bathymetric barriers on the slope. Topography generated by thrust faults and folds propagated gradually, leading to the formation of thickening-upward and coarsening-upward successions within growth-synclinal folds from thin-bedded mudstones to thick-bedded sandstones as topography generation outpaced sediment supply. When fold and thrust propagation became inactive, infill of the depocentres outpaced topography generation and deposits became progressively thinner bedded and finer grained. When bathymetric barriers were at their maximum vertical extent, rapid sedimentation resulted in up-flow accreting packages comparable to bedforms in supercritical flow deposits at channel-lobe transition zones and other areas of abrupt change in seabed topography.

This high-resolution outcrop study illustrates the complex kinematics and longevity of mass-transport deposit emplacement and how this influences subsequent sediment routing and deposition. It demonstrates that interpretation of facies successions in deep-water settings could easily be misinterpreted as the product of other submarine slope processes (for example, channel migration/avulsion, lobe compensational stacking) or allogenic controls, which in turn would affect palaeogeographic reconstructions.

ACKNOWLEDGEMENTS

This work was funded by the Natural Environment Research Council (NERC) as part of the Centre for Doctoral Training (CDT) programme. We thank James Lovell-Kennedy, Daniel Tek, Max Bouwmeester, Alfie Mackie and Yorick Veenma for their assistance in the field. We also thank Cai Puigdefàbregas for

valuable discussions and sharing his knowledge on the wider geology of the area. Finally, we thank reviewers David Hodgson and Kei Ogata for their in-depth and constructive reviews which substantially improved the manuscript.

REFERENCES

Allen, C., **Gomis-Cartesio, L.E.**, **Hodgson, D.M.**, **Peakall, J.** and **Milana, J.-P.** (2022) Channel incision into a submarine landslide on a Carboniferous basin margin, San Juan, Argentina: Evidence for the role of knickpoints. *The Depositional Record*, **8**, 628–655.

Allen, J.R.L. (1982) Sedimentary Structures: Their Character and Physical Basis. *Elsevier*, Amsterdam, 592 pp.

Armitage, D.A., **Romans, B.W.**, **Covault, J.A.** and **Graham, S.A.** (2009) The Influence of Mass-Transport-Deposit Surface Topography on the Evolution of Turbidite Architecture: The Sierra Contreras, Tres Pasos Formation (Cretaceous), Southern Chile. *Journal of Sedimentary Research*, **79**, 287–301.

Beaumont, C., **Muñoz, J.A.**, **Hamilton, J.** and **Fullsack, P.** (2000) Factors controlling the Alpine evolution of the central Pyrenees inferred from a comparison of observations and geodynamical models. *J Geophys Res Solid Earth*, **105**, 8121–8145.

Bell, D., **Stevenson, C.J.**, **Kane, I.A.**, **Hodgson, D.M.** and **Poyatos-Moré, M.** (2018) Topographic Controls On the Development of Contemporaneous but Contrasting Basin-Floor Depositional Architectures. *Journal of Sedimentary Research*, **88**, 1166–1189.

Bersezio, R., **Felletti, F.** and **Micucci, L.** (2005) Statistical analysis of stratal patterns and facies changes at the terminations of "turbiditic" sandstone bodies: The Oligocene Cengio Unit (Tertiary Piedmont Basin). *GeoActa*, **4**, 83–104.

Bhattacharya, J.P. and **MacEachern, J.A.** (2009) Hyperpycnal Rivers and Prodeltaic Shelves in the Cretaceous Seaway of North America. *Journal of Sedimentary Research*, **79**, 184–209.

Booth, J.R., **DuVernay, A.E.**, **Pfeiffer, D.S.** and **Styzen, M.J.** (2000) Sequence Stratigraphic Framework, Depositional Models, and Stacking Patterns of Ponded and Slope Fan Systems in the Auger Basin: Central Gulf of Mexico Slope. In: *Deep-Water Reservoirs of the World*, Volume 20 (Ed. P. Weimer), *SEPM Society for Sedimentary Geology*, 82–103.

Boulesteix, K., **Poyatos-Moré, M.**, **Flint, S.S.**, **Hodgson, D.M.**, **Taylor, K.T.** and **Brunt, R.L.** (2022) Sedimentologic and stratigraphic criteria to distinguish between basin-floor and slope mudstones: Implications for the delivery of mud to deep-water environments. *The Depositional Record*, **8**, 958–988.

Braathen, A., **Midtkandal, I.**, **Mulrooney, M.J.**, **Appleyard, T.R.**, **Haile, B.G.** and **van Yperen, A.E.** (2018) Growth-faults from delta collapse – structural and sedimentological investigation of the Last Chance delta, Ferron Sandstone, Utah. *Basin Research*, **30**, 688–707.

Brooks, H.L., **Hodgson, D.M.**, **Brunt, R.L.**, **Peakall, J.** and **Flint, S.S.** (2017) Exhumed lateral margins and increasing flow confinement of a submarine landslide complex. *Sedimentology*, **65**, 1067–1096.

Brooks, H.L., **Hodgson, D.M.**, **Brunt, R.L.**, **Peakall, J.**, **Poyatos-Moré, M.** and **Flint, S.S.** (2018) Disconnected submarine lobes as a record of stepped slope evolution over multiple sea-level cycles. *Geosphere*, **14**, 1753–1779.

Brunt, R.L., **McCaffrey, W.D.** and **Kneller, B.C.** (2004) Experimental Modeling of the Spatial Distribution of Grain Size Developed in a Fill-and-Spill Mini-Basin Setting. *Journal of Sedimentary Research*, **74**, 438–446.

Bull, S., **Browne, G.H.**, **Arnot, M.J.** and **Strachan, L.J.** (2020) Influence of mass transport deposit (MTD) surface topography on deep-water deposition: an example from a predominantly fine-grained continental margin, New Zealand. *Geological Society, London, Special Publications*, **500**, 147–171.

Bull, S., **Cartwright, J.** and **Huuse, M.** (2009) A review of kinematic indicators from mass-transport complexes using 3D seismic data. *Mar Pet Geol*, **26**, 1132–1151.

Burbank, D.W., **Puigdefàbregas, C.** and **Muñoz, J.A.** (1992) The chronology of the Eocene tectonic and stratigraphic development of the eastern Pyrenean foreland basin, northeast Spain. *GSA Bulletin*, **104**, 1101–1120.

Butler, R.W.H. and **McCaffrey, W.D.** (2010) Structural evolution and sediment entrainment in mass-transport complexes: Outcrop studies from Italy. *J Geol Soc London*, **167**, 617–631.

Butler, R.W.H. and **Paton, D.A.** (2010) Evaluating lateral compaction in deepwater fold and thrust belts: How much are we missing from "nature's sandbox"? *GSA Today*, **20**, 4–10.

Cantalejo, B. and **Pickering, K.T.** (2015) Orbital forcing as principal driver for fine-grained deep-marine siliciclastic sedimentation, Middle-Eocene Ainsa Basin, Spanish Pyrenees. *Palaeogeogr Palaeoclimatol Palaeoecol*, **421**, 24–47.

Carey, J.M., **Crutchley, G.J.**, **Mountjoy, J.J.**, **Petley, D.N.**, **McSaveney, M.J.** and **Lyndsell, B.** (2019) Slow episodic movement driven by elevated pore-fluid pressures in shallow subaqueous slopes. *Geomorphology*, **329**, 99–107.

Cartigny, M.J.B., **Ventra, D.**, **Postma, G.** and **van Den Berg, J.H.** (2014) Morphodynamics and sedimentary structures of bedforms under supercritical-flow conditions: New insights from flume experiments. *Sedimentology*, **61**, 712–748.

Casciano, C.I., **Patacci, M.**, **Longhitano, S.G.**, **Tropeano, M.**, **McCaffrey, W.D.** and **Di Celma, C.** (2019) Multi-scale analysis of a migrating submarine channel system in a tectonically-confined basin: The Miocene Gorgoglione Flysch Formation, southern Italy. *Sedimentology*, **66**, 205–240.

Castelltort, S., **Honegger, L.**, **Adatte, T.**, **Fildani, A.**, **Clark, J.D.**, **Dykstra, M.L.**, **Puigdefàbregas, C.**, **Spangenberg, J.E.**, **Honegger, L.**, **Adatte, T.**, **Clark, J.D.**, **Dykstra, M.L.**, **Puigdefàbregas, C.**, **Spangenberg, J.E.** and **Fildani, A.** (2017) Detecting eustatic and tectonic signals with carbon isotopes in deep-marine strata, Eocene Ainsa Basin, Spanish Pyrenees. *Geology*, **45**, 707–710.

Chanvry, E., **Deschamps, R.**, **Joseph, P.**, **Puigdefàbregas, C.**, **Poyatos-Moré, M.**, **Serra-Kiel, J.**, **Garcia, D.** and **Teinturier, S.** (2018) The influence of intrabasinal tectonics in the stratigraphic evolution of piggyback basin fills: Towards a model from the Tremp-Graus-Ainsa Basin (South-Pyrenean Zone, Spain). *Sediment Geol*, **377**, 34–62.

Chima, K.I., **Granjeon, D.**, **Couto, D. Do**, **Leroux, E.**, **Gorini, C.**, **Rabineau, M.**, **Letouzey, J.**, **Hoggmascall, N.** and **Glukstad, M.M.** (2022) Tectono-stratigraphic evolution of the offshore western Niger Delta from the Cretaceous to present: Implications of delta dynamics and paleo-topography on gravity-driven deformation. *Basin Research*, **34**, 25–49.

Clark, J.D., **Puigdefàbregas, C.**, **Castelltort, S.** and **Andrea, F.** (2017) Propagation of Environmental Signals within Source-to-Sink Stratigraphy. In: *SEPM Field Trip Guidebook 13*, *SEPM (Society for Sedimentary Geology)*, 1–124.

Covault, J.A., **Kostic, S.**, **Paull, C.K.**, **Sylvester, Z.** and **Fildani, A.** (2017) Cyclic steps and related supercritical bedforms: Building blocks of deep-water depositional systems, western North America. *Mar Geol*, **393**, 4–20.

Dalton, T.J.S., **Paton, D.A.** and **Needham, D.T.** (2017) Influence of mechanical stratigraphy on multi-layer gravity collapse structures: insights from the Orange Basin, South Africa. Petroleum Geoscience of the West Africa Margin, *The Geological Society of London*, **438**, 211–228.

Frey-Martínez, J., **Cartwright, J.** and **James, D.** (2006) Frontally confined versus frontally emergent submarine landslides: A 3D seismic characterisation. *Mar Pet Geol*, **23**, 585–604.

Heard, T.G., **Pickering, K.T.** and **Clark, J.D.** (2014) Ichnofabric characterization of a deep-marine clastic system: A subsurface study of the Middle Eocene Ainsa System, Spanish Pyrenees. *Sedimentology*, **61**, 1298–1331.

Helland-Hansen, W. and **Hampson, G.J.** (2009) Trajectory analysis: Concepts and applications. *Basin Research*, **21**, 454–483.

Hodgson, D.M., **Brooks, H.L.**, **Ortiz-Karpf, A.**, **Spychala, Y.**, **Lee, D.R.** and **Jackson, C.A.L.** (2018) Entrainment and abrasion of megaclasts during submarine landsliding and their impact on flow behaviour. In: *8th International Symposium on Submarine Mass Movements and Their Consequences, ISSMMTC 2018*, *The Geological Society of London*, 223–240.

Hodgson, D.M. and **Haughton, P.D.W.** (2004) Impact of syndepositional faulting on gravity current behaviour and deep-water stratigraphy: Tabernas-Sorbas Basin, SE Spain. *Geological Society, London, Special Publications*, **222**, 135 LP – 158.

Hodgson, D.M., **Kane, I.A.**, **Flint, S.S.**, **Brunt, R.L.** and **Ortiz-Karpf, A.** (2016) Time-transgressive confinement on the slope and the progradation of basin-floor fans: Implications for the sequence stratigraphy of deep-water deposits. *Journal of Sedimentary Research*, **86**, 73–86.

Howlett, D.M., **Ge, Z.**, **Nemec, W.**, **Gawthorpe, R.L.**, **Rotevatn, A.** and **Jackson, C.A.-L.** (2019) Response of unconfined turbidity current to deep-water fold and thrust belt topography: Orthogonal incidence on solitary and segmented folds. *Sedimentology*, **66**, 2425–2454.

Hubbard, S.M., **Covault, J.A.**, **Fildani, A.** and **Romans, B.W.** (2014) Sediment transfer and deposition in slope channels: Deciphering the record of enigmatic deep-sea processes from outcrop. *GSA Bulletin*, **126**, 857–871.

Hughes Clarke, J.E. (2016) First wide-angle view of channelized turbidity currents links migrating cyclic steps to flow characteristics. *Nat Commun*, **7**, 11896.

Jobe, Z., **Sylvester, Z.**, **Bolla Pittaluga, M.**, **Frascati, A.**, **Pirmez, C.**, **Minisini, D.**, **Howes, N.** and **Cantelli, A.** (2017) Facies architecture of submarine-channel deposits on the western Niger Delta slope: Implications for grain-size and density stratification in turbidity currents. *J Geophys Res Earth Surf*, **122**, 473–491.

Jobe, Z.R., **Lowe, D.R.** and **Morris, W.R.** (2012) Climbing-ripple successions in turbidite systems: depositional environments, sedimentation rates and accumulation times. *Sedimentology*, **59**, 867–898.

Kane, I.A., **Dykstra, M.L.**, **Kneller, B.C.**, **Tremblay, S.** and **McCaffrey, W.D.** (2009) Architecture of a coarse-grained channel–levée system: the Rosario Formation, Baja California, Mexico. *Sedimentology*, **56**, 2207–2234.

Kane, I.A., **Pontén, A.S.M.**, **Vangdal, B.**, **Eggenhuisen, J.T.**, **Hodgson, D.M.** and **Spychala, Y.T.** (2017) The stratigraphic record and processes of turbidity current transformation across deep-marine lobes. *Sedimentology*, **64**, 1236–1273.

Kneller, B.C. (1995) Beyond the turbidite paradigm: physical models for deposition of turbidites and their implications for reservoir prediction. *Geological Society, London, Special Publications*, **94**, 31–49.

Kneller, B.C. and **Branney, M.J.** (1995a) Sustained high-density turbidity currents and the deposition of thick massive sands. *Sedimentology*, **42**, 607–616.

Kneller, B.C. and **Branney, M.J.** (1995b) Sustained high-density turbidity currents and the deposition of thick massive sands. *Sedimentology*, **42**, 607–616.

Kneller, B.C., **Dykstra, M.L.**, **Fairweather, L.** and **Milana, J.P.** (2016) Mass-transport and slope accommodation: Implications for turbidite sandstone reservoirs. *Am Assoc Pet Geol Bull*, **100**, 213–235.

Kremer, C.H., **McHargue, T.**, **Scheucher, L.** and **Graham, S.A.** (2018) Transversely-sourced mass-transport deposits and stratigraphic evolution of a foreland submarine channel system: Deep-water tertiary strata of the Austrian Molasse Basin. *Mar Pet Geol*, **92**, 1–19.

Lewis, K.B. (1971) Slumping on a continental slope inclined at 1°–4°. *Sedimentology*, **16**, 97–110.

Lowe, D.R. (1982) Sediment gravity flows; II, Depositional models with special reference to the deposits of high-density turbidity currents. *Journal of Sedimentary Research*, **52**, 279–297.

Macdonald, H.A., **Peakall, J.**, **Wignall, P.B.** and **Best, J.** (2011) Sedimentation in deep-sea lobe-elements: implications for the origin of thickening-upward sequences. *J Geol Soc London*, **168**, 319 LP – 332.

Marini, M., **Milli, S.**, **Ravnås, R.** and **Moscatelli, M.** (2015) A comparative study of confined vs. semi-confined turbidite lobes from the Lower Messinian Laga Basin (Central Apennines, Italy): Implications for assessment of reservoir architecture. *Mar Pet Geol*, **63**, 142–165.

Martínez-Doñate, A., **Privat, A.M.-L.J.**, **Hodgson, D.M.**, **Jackson, C.A.-L.**, **Kane, I.A.**, **Spychala, Y.T.**, **Duller, R.A.**, **Stevenson, C.**, **Keavney, E.**, **Schwarz, E.** and **Flint, S.S.** (2021) Substrate Entrainment, Depositional Relief, and Sediment Capture: Impact of a Submarine Landslide on Flow Process and Sediment Supply. *Front. Earth Sci.,* **9**(757617), 1–23.

Millington, J.J. and **Clark, J.D.** (1995) The Charo/Arro canyon-mouth sheet system, south-central Pyrenees, Spain; a structurally influenced zone of sediment dispersal. *Journal of Sedimentary Research*, **65**, 443–454.

Mulder, T., **Syvitski, J.P.M.**, **Migeon, S.**, **Faugères, J.-C.** and **Savoye, B.** (2003) Marine hyperpycnal flows: initiation, behavior and related deposits. A review. *Mar Pet Geol*, **20**, 861–882.

Muñoz, J.A. (2002) The Pyrenees. In: *The Geology of Spain* (Ed. W. Gibbons and T. Moreno), *Geological Society, London*, 370–385.

Muñoz, J.A., **Beamud, E.**, **Fernández, O.**, **Arbués, P.**, **Dinarès-Turell, J.** and **Poblet, J.** (2013) The Ainsa Fold and thrust oblique zone of the central Pyrenees: Kinematics of a curved contractional system from paleomagnetic and structural data. *Tectonics*, **32**, 1142–1175.

Mutti, E. (1977) Distinctive thin-bedded turbidite facies and related depositional environments in the Eocene Hecho Group (South-central Pyrenees, Spain). *Sedimentology*, **24**, 107–131.

Mutti, E. (1992) Turbidite sandstones. *San Donato Milanese: Istituto di Geologia, Universit`a di Parma*, 275 pp.

Mutti, E. (2019) Thin-bedded plumites : an overlooked deep-water deposit. *Journal of Mediterranean Earth Sciences*, **11**, 20.

Mutti, E., **Luterbacher, H.P.**, **Ferrer, J.** and **Rosell, J.** (1972) Schema stratigrafico e lineamenti di facies del Paleogene marino della zona centrale sudpirenaica tra temp (Catalogna) e Pamplona (Navarra). *Memorie della società geologica italiana*, **11**, 391–416.

Mutti, E. and **Normark, W.R.** (1987) Comparing Examples of Modern and Ancient Turbidite Systems: Problems and Concepts. *Marine Clastic Sedimentology*, 1–38.

Mutti, E., **Remacha, E.**, **Scavetti, M.**, **Rosell, J.**, **Valloni, R.** and **Zamorano, M.** (1985) Stratigraphy and Facies Characteristics of the Eocene Hecho Group Turbidite Systems, South-central Pyrenees. In: *MILA, M.D. and ROSELL, J. (Eds.): 6th IAS European regional Meeting, Lleida*, *IAS*, 519–576.

Nijman, W. (1998) Cyclicity and basin axis shift in a piggyback basin: towards modelling of the Eocene Tremp-Ager Basin, South Pyrenees, Spain. *Geological Society, London, Special Publications*, **134**, 135 LP – 162.

Nwoko, J., **Kane, I.A.** and **Huuse, M.** (2020) Mass transport deposit (MTD) relief as a control on post-MTD sedimentation: Insights from the Taranaki Basin, offshore New Zealand. *Mar Pet Geol*, **120**, 1–27.

Nyberg, B., **Helland-Hansen, W.**, **Gawthorpe, R.L.**, **Sandbakken, P.**, **Eide, C.H.**, **Sømme, T.**, **Hadler-Jacobsen, F.** and **Leiknes, S.** (2018) Revisiting morphological relationships of modern source-to-sink segments as a first-order approach to scale ancient sedimentary systems. *Sediment Geol*, **373**, 111–133.

Odonne, F., **Callot, P.**, **Debroas, E.-J.**, **Sempere, T.**, **Hoareau, G.** and **Maillard, A.** (2011) Soft-sediment deformation from submarine sliding: Favourable conditions and triggering mechanisms in examples from the Eocene Sobrarbe delta (Ainsa, Spanish Pyrenees) and the mid-Cretaceous Ayabacas Formation (Andes of Peru). *Sediment Geol*, **235**, 234–248.

Ogata, K., **Mutti, E.**, **Pini, G.A.** and **Tinterri, R.** (2012) Mass transport-related stratal disruption within sedimentary mélanges: Examples from the northern Apennines (Italy) and south-central Pyrenees (Spain). *Tectonophysics*, **568–569**, 185–199.

Ortiz-Karpf, A., **Hodgson, D.M.**, **Jackson, C.A.-L.** and **McCaffrey, W.D.** (2018) Mass-transport complexes as markers of deep-water fold-and-thrust belt evolution: insights from the southern Magdalena fan, offshore Colombia. *Basin Research*, **30**, 65–88.

Ortiz-Karpf, A., **Hodgson, D.M.**, **Jackson, C.A.-L.** and **McCaffrey, W.D.** (2017) Influence of Seabed Morphology and Substrate Composition On Mass-Transport Flow Processes and Pathways: Insights From the Magdalena Fan, Offshore Colombia. *Journal of Sedimentary Research*, **87**, 189–209.

Ortiz-Karpf, A., **Hodgson, D.M.** and **McCaffrey, W.D.** (2015) The role of mass-transport complexes in controlling channel avulsion and the subsequent sediment dispersal patterns on an active margin: The Magdalena Fan, offshore Colombia. *Mar Pet Geol*, **64**, 58–75.

Payros, A., **Tosquella, J.**, **Bernaola, G.**, **Dinarès-Turell, J.**, **Orue-Etxebarria, X.** and **Pujalte, V.** (2009) Filling the North European Early/Middle Eocene (Ypresian/Lutetian) boundary gap: Insights from the Pyrenean continental to deep-marine record. *Palaeogeogr Palaeoclimatol Palaeoecol*, **280**, 313–332.

Peakall, J., **Best, J.**, **Baas, J.H.**, **Hodgson, D.M.**, **Clare, M.A.**, **Talling, P.J.**, **Dorrell, R.M.** and **Lee, D.R.** (2020) An integrated process-based model of flutes and tool marks in deep-water environments: Implications for palaeohydraulics, the Bouma sequence and hybrid event beds. *Sedimentology*, **67**, 1601–1666.

Pickering, K.T. and **Bayliss, N.J.** (2009) Deconvolving tectono-climatic signals in deep-marine siliciclastics, Eocene Ainsa basin, Spanish Pyrenees: Seesaw tectonics versus eustasy. *Geology*, **37**, 203–206.

Pohl, F., **Eggenhuisen, J.T.**, **Cartigny, M.J.B.**, **Tilston, M.**, **de Leeuw, J.** and **Hermidas, N.** (2020) The influence of a slope break on turbidite deposits: An experimental investigation. *Mar Geol.*, **424**,1–22

Postma, G. and **Cartigny, M.J.B.** (2014) Supercritical and subcritical turbidity currents and their deposits—A synthesis. *Geology*, **42**, 987–990.

Poyatos-Moré, M. (2014) Physical Stratigraphy and Facies Analysis of the Castissent Tecto-Sedimentary Unit (South-Central Pyrenees, Spain). PhD thesis. Universidad Autónoma de Barcelona. 1–282.

Poyatos-Moré, M., **Jones, G.E.D.**, **Brunt, R.L.**, **Hodgson, D.M.**, **Wild, R.J.** and **Flint, S.S.** (2016) Mud-Dominated Basin-Margin Progradation: Processes and Implications. *Journal of Sedimentary Research*, **86**, 863–878.

Prather, B. (2000) Calibration and visualization of depositional process models for above-grade slopes: a case study from the Gulf of Mexico. *Mar Pet Geol*, **17**, 619–638.

Prather, B., **Booth, J.R.**, **Steffens, G.S.** and **Craig, P.A.** (1998) Classification, Lithologic Calibration, and Stratigraphic Succession of Seismic Facies of Intraslope Basins, Deep-Water Gulf of Mexico. *Am Assoc Pet Geol Bull*, **82 (1998)**, 34–60.

Prather, B. (2003) Controls on reservoir distribution, architecture and stratigraphic trapping in slope settings. *Mar Pet Geol*, **20**, 529–545.

Prather B, **O'Byrne, C.**, **Pirmez, C.** and **Sylvester, Z.** (2017) Sediment partitioning, continental slopes and base-of-slope systems. *Basin Research*, **29**, 394–416.

Prélat, A., **Hodgson, D.M.** and **Flint, S.S.** (2009) Evolution, architecture and hierarchy of distributary deep-water deposits: a high-resolution outcrop investigation from the Permian Karoo Basin, South Africa. *Sedimentology*, **56**, 2132–2154.

Remacha, E., **Gual, G.**, **Bolaño, F.**, **Arcuri, M.**, **Oms, O.**, **Climent, F.**, **Crumeyrolle, P.**, **Fernández, L.P.**, **Vicente, J.C.** and **Suarez, J.** (2003) Sand-rich turbidite systems of the Hecho Group from slope to basin plain; facies, stacking patterns, controlling factors and diagnostic features. Geological field trip 12: Field Guide 2, 1–70.

Rosenbaum, G., **Lister, G.S.** and **Duboz, C.** (2002) Relative motions of Africa, Iberia and Europe during Alpine orogeny. *Tectonophysics*, **359**, 117–129.

Ross, W.C., **Halliwell, B.A.**, **May, J.A.**, **Watts, D.E.** and **Syvitski, J.P.M.** (1994) Slope readjustment: A new model for the development of submarine fans and aprons. *Geology*, **22**, 511–514.

Ross, W.C., **Watts, D.E.** and **May, J.A.** (1995) Insights from stratigraphic modeling: mud-limited versus sand- limited depositional systems. *American Association of Petroleum Geologists Bulletin*, **79**, 231–258.

Rowan, M.G., **Peel, F.J.** and **Vendeville, B.C.** (2004) Gravity-driven Fold Belts on Passive Margins. Thrust Tectonics and Hydrocarbon Systems **82**, 157–182.

Ryan, M.C., **Helland-Hansen, W.**, **Johannessen, E.P.** and **Steel, R.J.** (2009) Erosional vs. accretionary shelf margins: the influence of margin type on deepwater sedimentation: an example from the Porcupine Basin, offshore western Ireland. *Basin Research*, **21**, 676–703.

Sammartini, M., **Moernaut, J.**, **Anselmetti, F.S.**, **Hilbe, M.**, **Lindhorst, K.**, **Praet, N.** and **Strasser, M.** (2019) An Atlas of Mass-Transport Deposits in Lakes. Submarine Landslides 201–226.

Scotchman, J.I., **Bown, P.**, **Pickering, K.T.**, **BouDagher-Fadel, M.**, **Bayliss, N.J.** and **Robinson, S.A.** (2015) A new age model for the middle Eocene deep-marine Ainsa Basin, Spanish Pyrenees. *Earth Sci Rev*, **144**, 10–22

Shanmugam, G. (2019) Slides, Slumps, Debris Flows, Turbidity Currents, Hyperpycnal Flows, and Bottom Currents. In: *Encyclopedia of Ocean Sciences* (Ed. J.K. Cochran, H.J. Bokuniewicz, and P.L.B.T.-E. of O.S. (Third E. Yager), *Elsevier*, Oxford, 228–257.

Sinclair, H.D. (1994) The influence of lateral basinal slopes on turbidite sedimentation in the Annot sandstones of SE France. *Journal of Sedimentary Research*, **64**, 42–54.

Sinclair, H.D. and **Tomasso, M.** (2002) Depositional Evolution of Confined Turbidite Basins. *Journal of Sedimentary Research*, **72**, 451–456.

Soutter, E.L., **Bell, D.**, **Cumberpatch, Z.A.**, **Ferguson, R.A.**, **Spychala, Y.T.**, **Kane, I.A.** and **Eggenhuisen, J.T.** (2021) The Influence of Confining Topography Orientation on Experimental Turbidity Currents and Geological Implications. *Front. Earth Sci.*, **8**(540633), 1–25.

Soutter, E.L., **Kane, I.A.**, **Fuhrmann, A.**, **Cumberpatch, Z.A.** and **Huuse, M.** (2019) The stratigraphic evolution of onlap in siliciclastic deep-water systems: Autogenic modulation of allogenic signals. *Journal of Sedimentary Research*, **89**, 890–917.

Spychala, Y.T., **Hodgson, D.M.**, **Flint, S.S.** and **Mountney, N.P.** (2015) Constraining the sedimentology and stratigraphy of submarine intraslope lobe deposits using exhumed examples from the Karoo Basin, South Africa. *Sediment Geol*, **322**, 67–81.

Srivastava, S.P. and **Roest, W.R.** (1991) Kinematics of the plate boundaries between Eurasia, Iberia, and Africa in the North Atlantic from the Late Cretaceous to the present. *Geology*, **19**, 613–616.

Stevenson, C.J., **Jackson, C.A.-L.**, **Hodgson, D.M.**, **Hubbard, S.M.** and **Eggenhuisen, J.T.** (2015) Deep-Water Sediment Bypass. *Journal of Sedimentary Research*, **85**, 1058–1081.

Stevenson, C.J. and **Peakall, J.** (2010) Effects of topography on lofting gravity flows: Implications for the deposition of deep-water massive sands. *Mar Pet Geol*, **27**, 1366–1378.

Sumner, E.J., **Amy, L.A.** and **Talling, P.J.** (2008) Deposit Structure and Processes of Sand Deposition from Decelerating Sediment Suspensions. *Journal of Sedimentary Research*, **78**, 529–547.

Talling, P.J., **Masson, D.G.**, **Sumner, E.J.** and **Malgesini, G.** (2012) Subaqueous sediment density flows: Depositional processes and deposit types. *Sedimentology*, **59**, 1937–2003.

Talling, P.J., **Wynn, R.B.**, **Masson, D.G.**, **Frenz, M.**, **Cronin, B.T.**, **Schiebel, R.**, **Akhmetzhanov, A.M.**, **Dallmeier-Tiessen, S.**, **Benetti, S.**, **Weaver, P.P.E.**, **Georgiopoulou, A.**, **Zühlsdorff, C.** and **Amy, L.A.** (2007) Onset of submarine debris flow deposition far from original giant landslide. *Nature*, **450**, 541–544.

Tek, D.E., **McArthur, A.D.**, **Poyatos-Moré, M.**, **Colombera, L.**, **Allen, C.**, **Patacci, M.** and **McCaffrey, W.D.** (2022) Controls on the architectural evolution of deep-water channel overbank sediment wave fields: insights from the Hikurangi Channel, offshore New Zealand. *New Zealand Journal of Geology and Geophysics*, **65**, 141–178.

Tek, D.E., **McArthur, A.D.**, **Poyatos-Moré, M.**, **Colombera, L.**, **Patacci, M.**, **Craven, B.** and **McCaffrey, W.D.** (2021) Relating seafloor geomorphology to subsurface architecture: How mass-transport deposits and knickpoint-zones build the stratigraphy of the deep-water Hikurangi Channel. *Sedimentology*, **68**, 3141–3190.

Tek, D.E., **Poyatos-Moré, M.**, **Patacci, M.**, **McArthur, A.**, **Colombera, L.**, **Cullen, T.M.** and **McCaffrey, W.D.** (2020) Syndepositional tectonics and mass-transport deposits control channelized, bathymetrically complex deep-water systems (Aínsa depocenter, Spain). *Journal of Sedimentary Research*, **90**, 729–762.

Ward, N.I.P., **Alves, T.M.** and **Blenkinsop, T.G.** (2018) Submarine sediment routing over a blocky mass-transport deposit in the Espírito Santo Basin, SE Brazil. *Basin Research*, **30**, 816–834.

Wild, R.J., **Hodgson, D.M.** and **Flint, S.S.** (2005) Architecture and stratigraphic evolution of multiple, vertically-stacked slope channel complexes, Tanqua depocentre, Karoo Basin, South Africa. *Geological Society, London, Special Publications*, **244**, 89 LP – 111.

Zavala, C. and **Pan, S.** (2018) Hyperpycnal flows and hyperpycnites：Origin and distinctive characteristics. *Lithologic Reservoirs*, **30**, 1–27.

DATA AVAILABILITY STATEMENT

The data that support the findings of this study are available from the corresponding author upon request.

FIGURE/TABLE CAPTIONS

Fig. 1. Schematic dip-parallel profile illustrating the topographic features generated by the evacuation and emplacement of mass-transport deposit (MTD), based on work by Shanmugam (2019) and Bull *et al.* (2020).

Fig. 2. (A) Map of Iberian peninsula highlighting the Pyrenees. (B) Structural map of the Pyrenees showing pre-orogenic basement, syn-orogenic and post-orogenic units and the main structures of the South-Central Unit (SCU) (after Muñoz *et al.*, 2013). (C) Palaeogeography of the South-Pyrenean Foreland Basin during the Upper Ypresian (after Dreyer *et al.*, 1999; Bell *et al.*, 2018). (D) Chronostratigraphy and lithostratigraphy of the Jaca, Aínsa and Tremp-Graus Basins. Tremp-Graus basin ages after Bentham and Burbank (1996) and Payros *et al.* (2009). Ages of Hecho Group deposits after Cantalejo *et al.* (2020). Correlations to Jaca Basin after Clark *et al.* (2017). Lithologies and unit names after Muñoz *et al.* (2013), Poyatos-Moré (2014), Clark *et al.* (2017) and Chanvry *et al.* (2018). (E) Schematic depositional dip-parallel profile of depositional environments at Castissent-Fosado-Tobacor equivalent time. LAS = Lascorz canyon; POC = Pocino canyon; AT = Atiart canyon; C1/C2 = Castissent formations 1 and 2; atcl. = anticline.

Fig. 3. Geological map of study area showing the position of the Barranco de Fosado Section and the Samper Ridge Section. A summary of facies associations, tectonic structures, bedding, average palaeoflow and average soft-sediment failure direction readings are shown. Contacts and faults beyond mapped area (coloured) after Clark *et al.* (2017). Bedding readings were used to plot form lines within the slope succession. Note the general north-west-

oriented palaeoflow direction, except locally in footwall on the Atiart Thrust. Growth of this structure is considered to have been synchronous with deposition.

Table 1. Lithofacies descriptions of the studied deposits. Bed thicknesses, grain size, lithologies, bedforms and process interpretations are presented. Photographs of each lithofacies are shown in Fig. 4

Fig. 4. Photographs of lithofacies described in Table 1, and examples of how these lithofacies stack into facies associations.

Fig. 5. Outcrop panel of the Barranco de Fosado Section (Fig. 3). (A) Three-dimensional outcrop model of the locality produced using photogrammetry. (B) A 2D projected panel of bed correlations using logs and the 3D outcrop model (link to raw model in footnotes). The 2D panel has been exaggerated vertically by a factor of x5 approximately. Minor post-depositional folding has been removed. (C) Location map showing local palaeoflow directions and rose diagrams for slope failure transport direction, normal fault dip and flute cast versus ripple palaeoflows.

Fig. 6. Simplified block diagrams depicting palaeogeography and formation of the Barranco de Fosado Section. Time divisions show a snapshot of each 'T' interval in Fig. 5. Basal shear plane inferred. The most dominant syn-depositional faults at each time interval are shown in bold lines.

Fig. 7. Outcrop panel of the Samper Ridge Section (Fig. 3). (A) Three-dimensional outcrop model of the locality produced using photogrammetry (link to raw model in footnotes). (B) Location map showing local palaeoflow directions and rose diagrams for slope failure transport direction, normal fault dip and flute cast vs ripple palaeoflows. (C) A 2D projected panel of bed correlations using logs and the 3D outcrop model. The 2D panel has been vertically exaggerated vertically by a factor of 16.

Fig. 8. Simplified block diagrams depicting palaeogeography and formation of the Samper Ridge Section. The orientation of the diagrams slightly differs to the panel in Fig. 7 to better show the structures in 3D. Time divisions show a snapshot of each 'T' interval in Fig. 5. Only three faults have been shown and their locations approximated for simplification. The most dominant syn-depositional faults at each time interval are bold.

Fig. 9. Thickening-up and coarsening-up succession seen in the synclinal depocentre recorded in log L8 (Fig 7) at the Samper Ridge Section. Upper deposits show aggradation surfaces that indicate up-slope migration. Cobble-sized mudstone rip-up clasts are suspended in upper sandstone deposits indicating up-dip erosion of the fine-grained substrate and rapid deposition of sediment.

Fig. 10. Impact of dynamic creeping topography on erosion and deposition of sediment gravity flow deposits from initiation to post-creep stages. A comparison is made between laterally confined (for example, the Barranco de Fosado Section) *versus* frontally confined (for example, the Samper Ridge Section) settings.

Fig. 11. Summary diagram showing the styles of topographic accommodation space generated above a mass-transport deposit (MTD) as seen in this study, morphology of MTD cross-section based on Bull *et al.* (2009). Turbidity currents prior to encountering MTD topography were likely broad and sheet-like on the slope rather than derived from a channelized point. Cross-sections and idealised vertical assemblages for extension and compression derived topographic features are presented. 1 = Barranco de Fosado Section equivalent; 2 = Samper Ridge Section equivalent. MTD derived topographic features are depicted here on a single, idealised MTD, data in this study was collected from outcrops of two different MTDs at a similar stratigraphic time interval.

Code	Lithofacies	Bed thickness	Grain size	Description	Interpretation
Lf1	Structureless mudstones	No distinct bedding or lamination	Clay dominated mudstone	No apparent grading. Often calcareous, weathers to form sub rounded-oval spheroids	Hemipelagic settling of sediment load suspended in water column
Lf2	Normally-graded mudstones	0.1–5.0 cm	Clay to silt mudstone, with rare very fine-grained sandstone	Very thin internal laminations, low amplitude (>1 mm) climbing ripple cross-lamination observed. Some low amplitude (>1 mm) starved ripples near bed tops. Often grading from silt to clay. Rare very fine sandstone grains scattered in bed or concentrated as basal level. Bed tops and bottoms can be difficult to distinguish from laminae	Deposits of decelerating low-concentration turbidity currents, with rare sandy grains at the bottom of beds representing lag of a predominantly bypassing flow (Stow & Shanmugam, 1980; Mutti & Normark, 1987; Stevenson *et al.*, 2015)
Lf3	Inverse and normal-graded mudstones	Laminae of 0.05–0.5 cm	Clay to silt mudstone, with rare	Thinly laminated mudstones to sandstones with no clear bed tops or bases. Laminations can be normal or inverse graded. Rarely contain very fine-grained sandstone	Deposition from sustained low-concentration turbidity currents, with internal 'waxing and waning' flow fluctuations (Mulder *et al.*,

			very fine-grained sandstone	laminae. Frequent occurrence of >0.5 mm plant fragments aligned within laminae	2003; Bhattacharya & MacEachern, 2009; Zavala & Pan, 2018)
Lf4	Thin-bedded rippled sandstones	0.5–10 cm	Very fine to fine-grained sandstone	Common planar and ripple cross-lamination with straight-crested current ripple tops and rare linguoid ripple tops. Beds are normally graded, and some can grade up to silt. The thinnest can form starved ripples. Beds often exhibit minor scours at the base preserved as flute, groove and gutter casts, and 'pinch and swell' in response to irregular topography in underling strata	Traction and deposition from dilute, initially bypassing, decelerating sediment gravity flows (Allen, 1982; Jobe *et al.*, 2012)
Lf5a	Normally-graded structureless sandstone	0.2–1.5 m	Very fine-grained sandstone to coarse-grained sandstone (rarely contains granules)	Ungraded to weakly normally graded from base to middle of bed. Infrequent sharp grading at very top of bed with ripple lamination and ripple top. Frequent minor scours at the base with flute and groove casts preserved. Muddy rip-up clasts and loaded flame structures are common at the base. Often show evidence of dewatering	Rapid deposition from a waning, high density turbidity current (Bouma, 1962; Lowe, 1982)

Lf5b	Massive sandstone	0.5–3.0 m	Very fine-grained to coarse-grained sandstone (rarely contains granules)	Thick, structureless and ungraded beds. Often exhibit intense internal deformation from dewatering. Minor scours at bed bases are common, with flute, groove and gutter casts. When staked or deposited on Lf5a beds this facies often forms amalgamation surfaces (sandstone on sandstone contacts) often marked by a band of rip-up mudstone clasts. Loaded flame structures are very common at the base	Rapid *en masse* deposition of an initially erosive, but rapidly decelerating, high density turbidity current (Lowe, 1982; Talling *et al.*, 2012)
MTDa	Cohesive, slide (slump)	0.5–15 m	Fine mudstone to coarse-grained sandstone	Moderately plastically deformed and folded beds of sandstone and mudstones of Lf1–Lf5a. Deposits recognized by their cohesive nature and not distinctly disaggregated. Folding often verges in palaeoslope dip direction. Deposits can exhibit extensive internal thrusting and normal faulting. Base of deposit often marked by an evacuation scar or on top of a debrite (MTDc)	Sliding and slumping of nearby stratigraphy, not remobilized very far (not disaggregated). Partial slump folding can also occur in heterolithic deposits on top of a mobile/creeping debrite (Ogata *et al.*, 2012; Shanmugam, 2019)

MTDb	Disaggregated, blocky deposit	0.5–15 m	Fine mudstone to coarse-grained sandstone	Extensively plastically deformed, folded and disaggregated clasts of Lf4–Lf5a, often contained within a chaotic mudstone matrix. Extensive internal thrusting and normal faulting is common	Disaggregated down-dip transition of MTDa, where slump folds become disaggregated and incorporated in to a blocky flow (Ogata *et al.*, 2012)
MTDc	Debris flow deposits (debrite)	0.1–30 m	Matrix: Fine-grained mudstone to fine-grained sandstone Clasts: Centimetre to metre scale blocks of hetrolithic packages, sandstones, carbonates and bioclasts	Chaotic mudstone matrix containing some plastically deformed sub-rounded blocks of disaggregated updip slope substrate material. Rafted blocks of shelf carbonate and heterolithic sandstone and mudstones packages can be found towards the top. Base of this deposit can be marked by a scoured contact	*En masse* deposition and 'freezing' of cohesive debris flows initiated by gravitational collapse, evacuation and disaggregation of substrate further up slope, including shelf material. The deposits of these flows are termed 'debrites' (Talling *et al.*, 2012; Shanmugam, 2019)

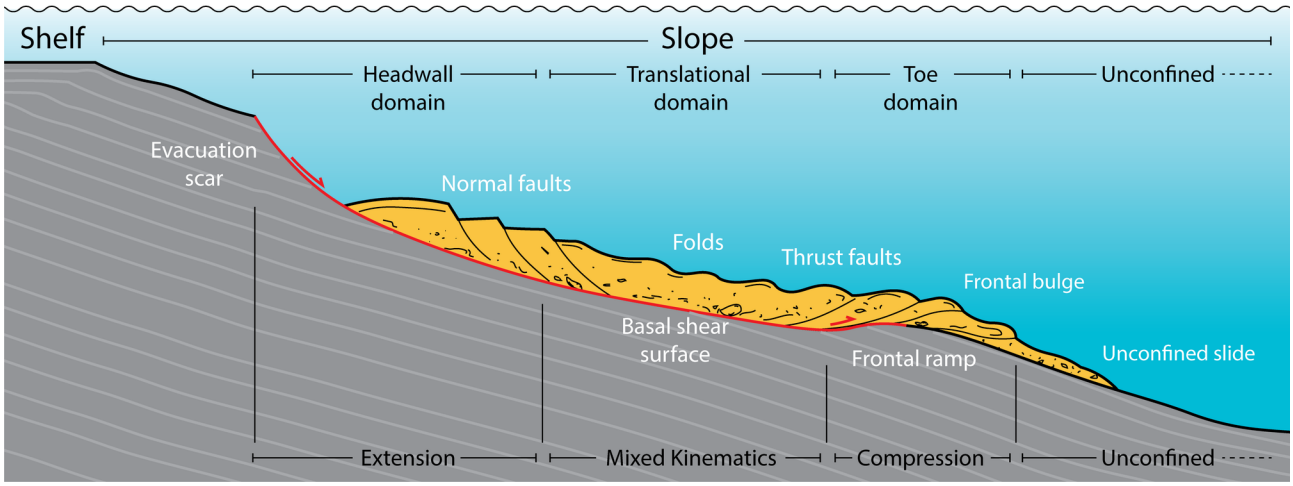

SED_13049_Fig. 1.tif

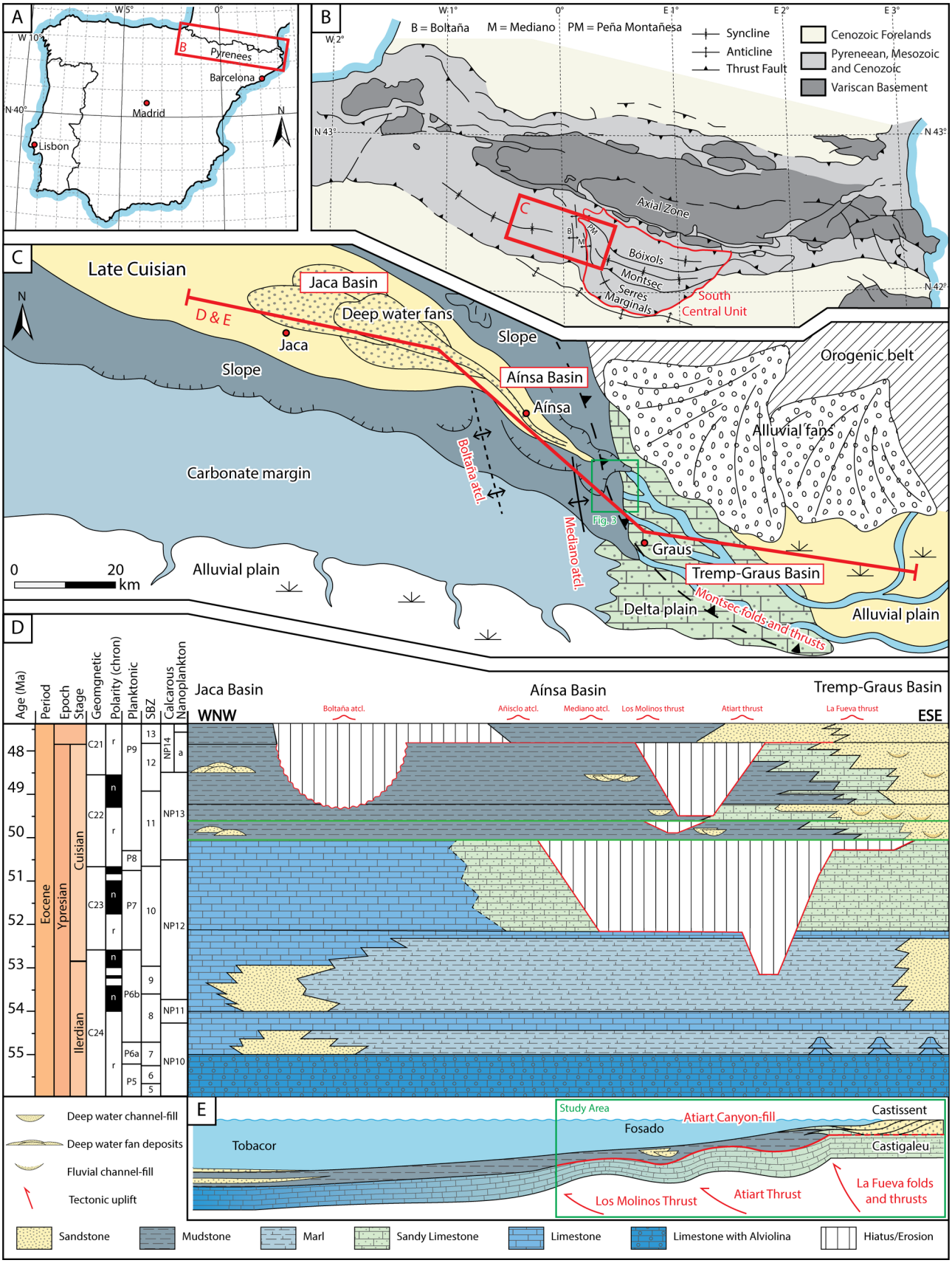

SED_13049_Fig. 2.tif

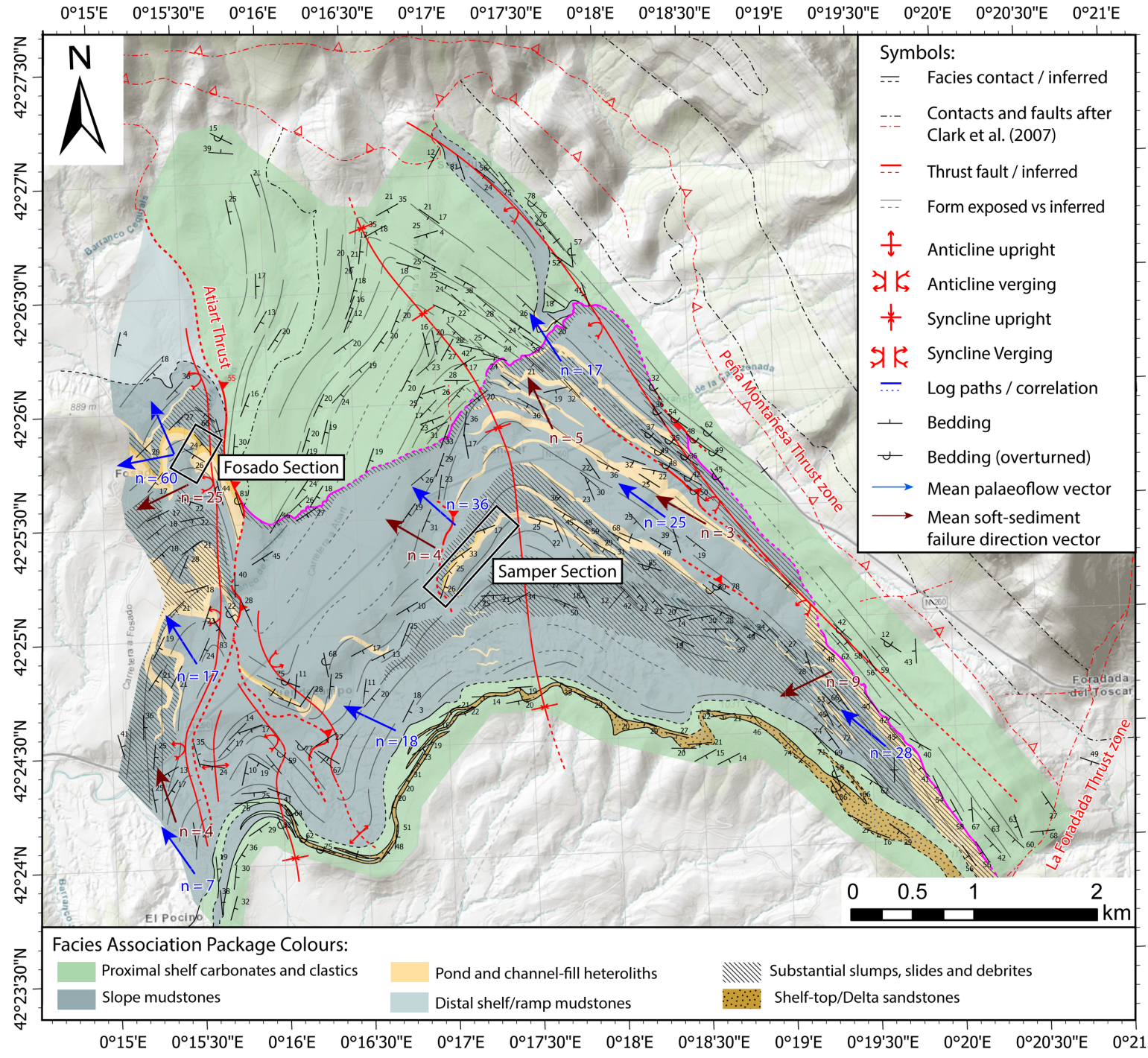

SED_13049_Fig. 3.tif

SED_13049_Fig. 4.tif

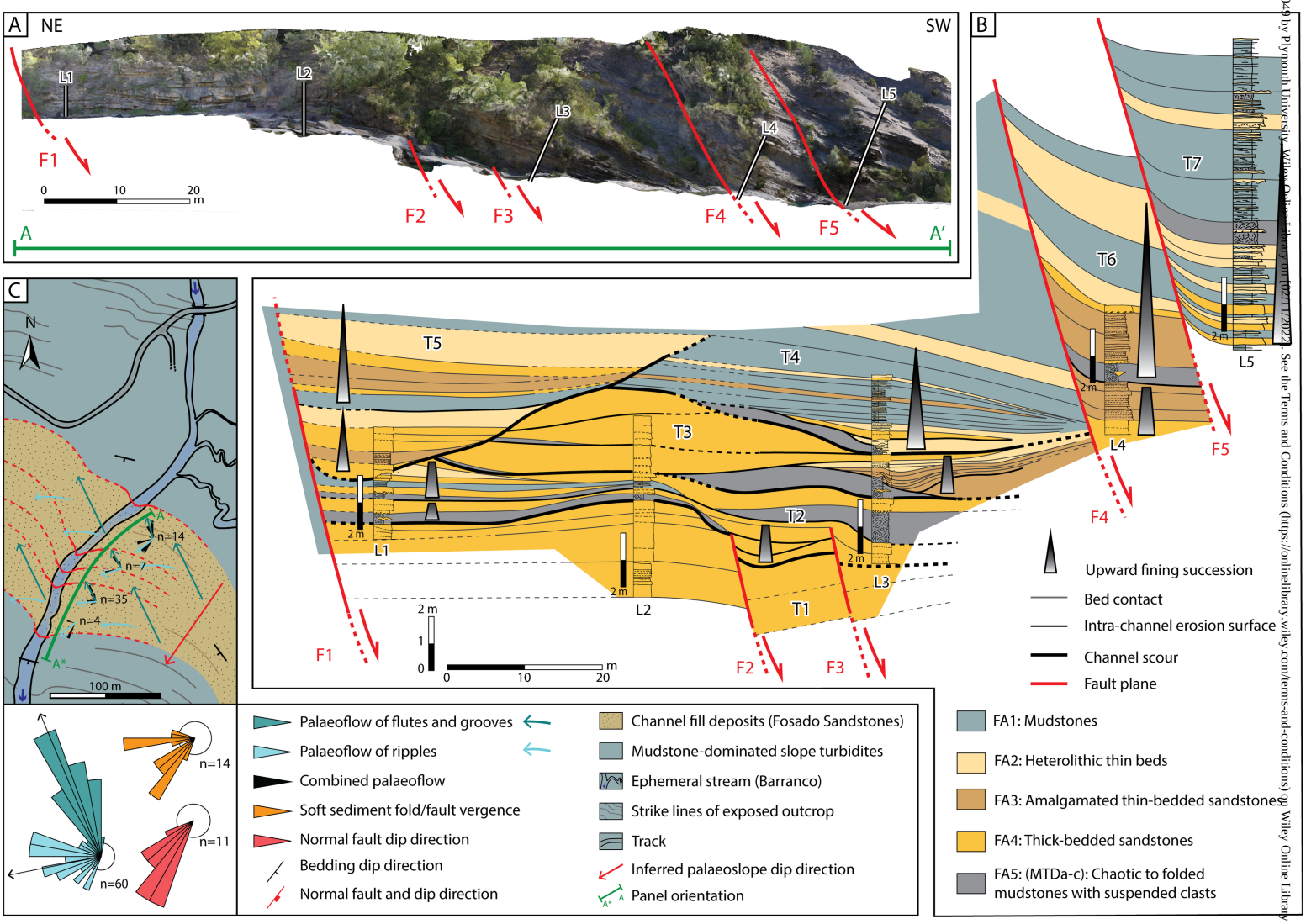

SED_13049_Fig. 5.tif

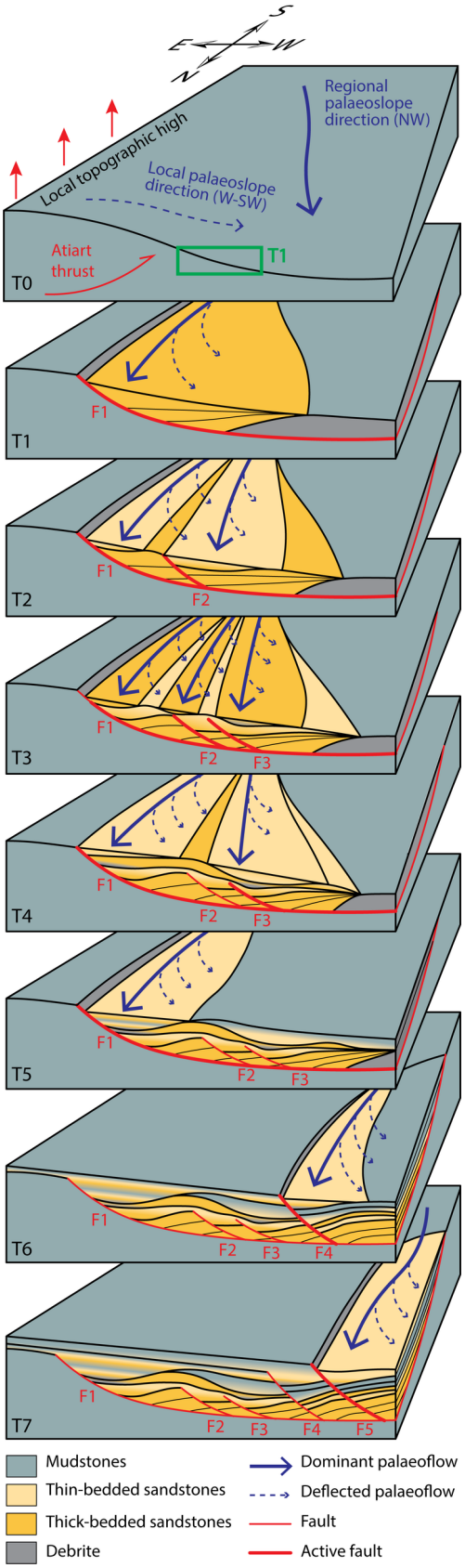

SED_13049_Fig. 6.tif

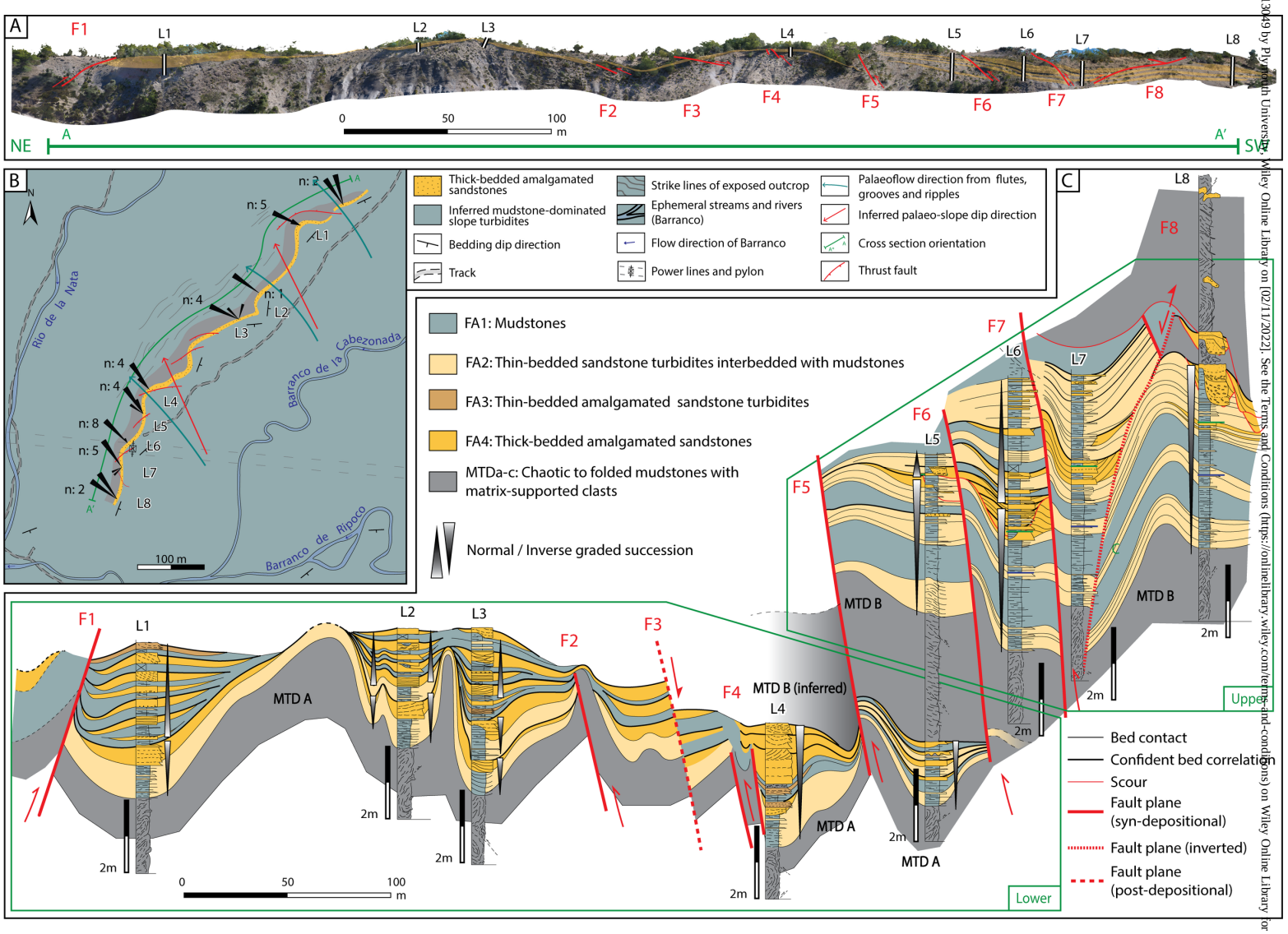

SED_13049_Fig. 7.tif

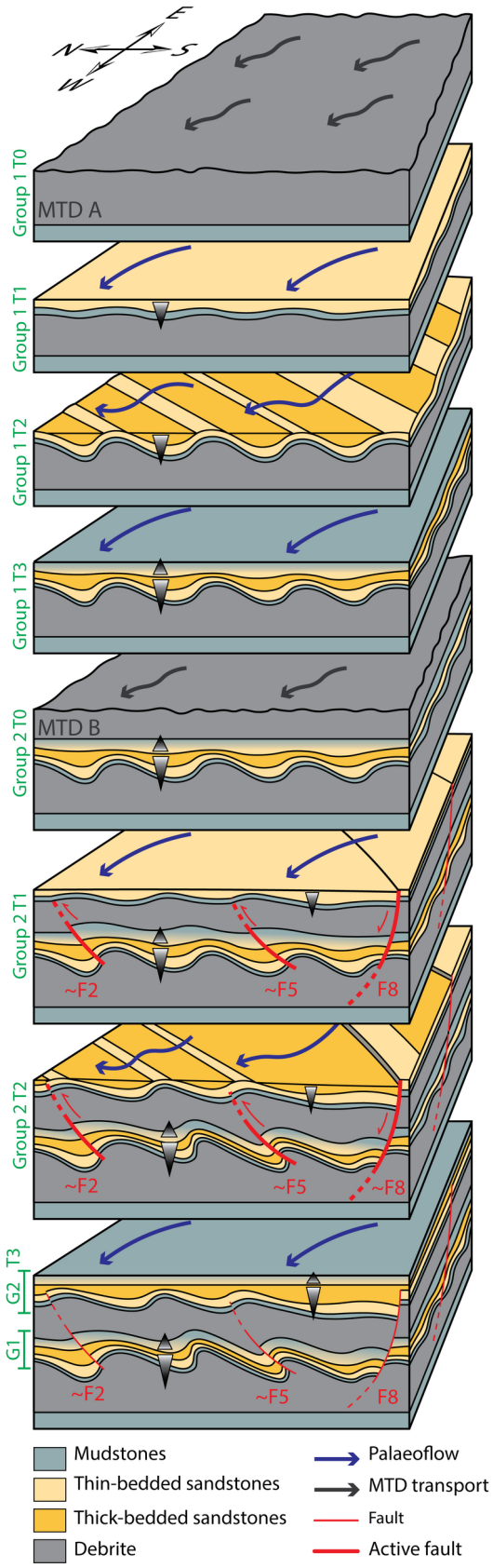

SED_13049_Fig. 8.tif

SED_13049_Fig. 9.tif

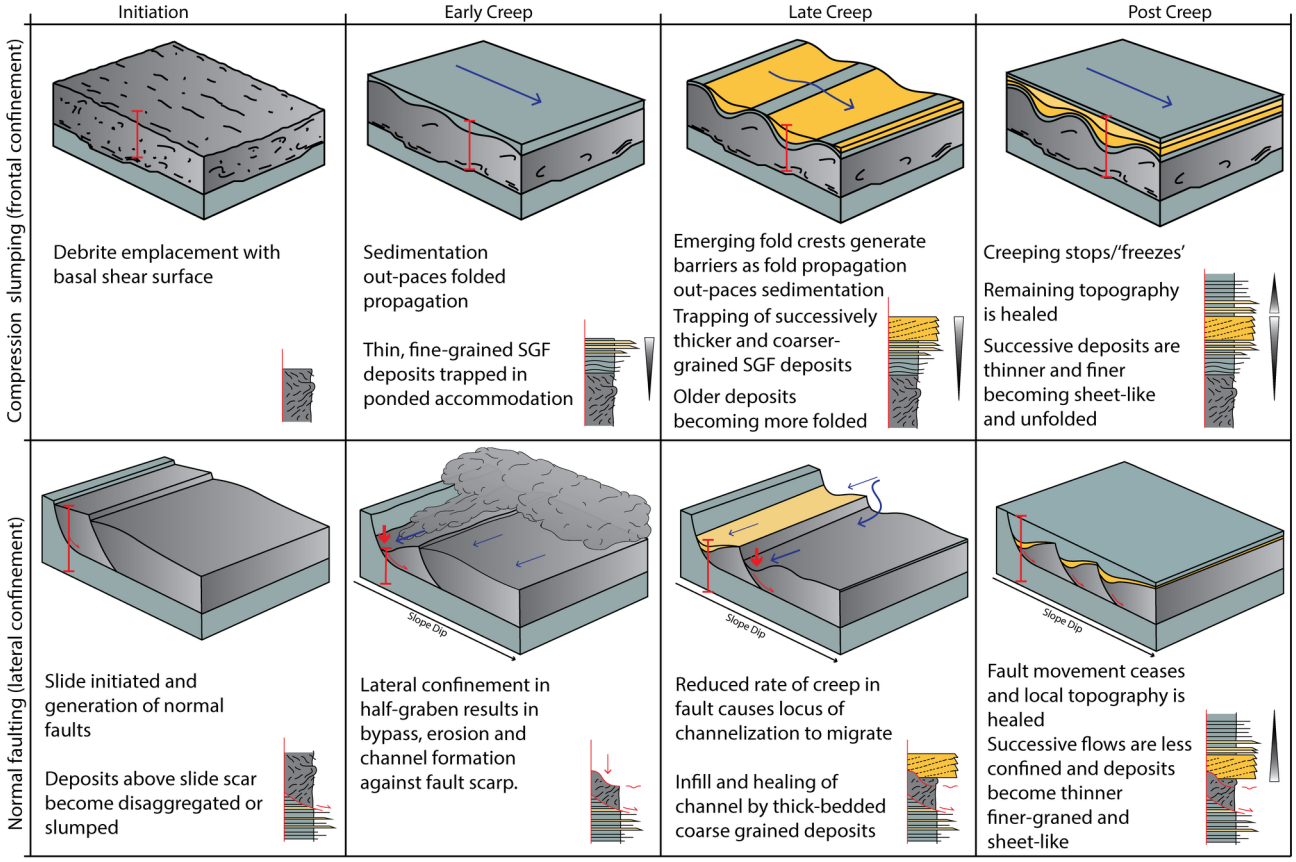

SED_13049_Fig. 10.tif

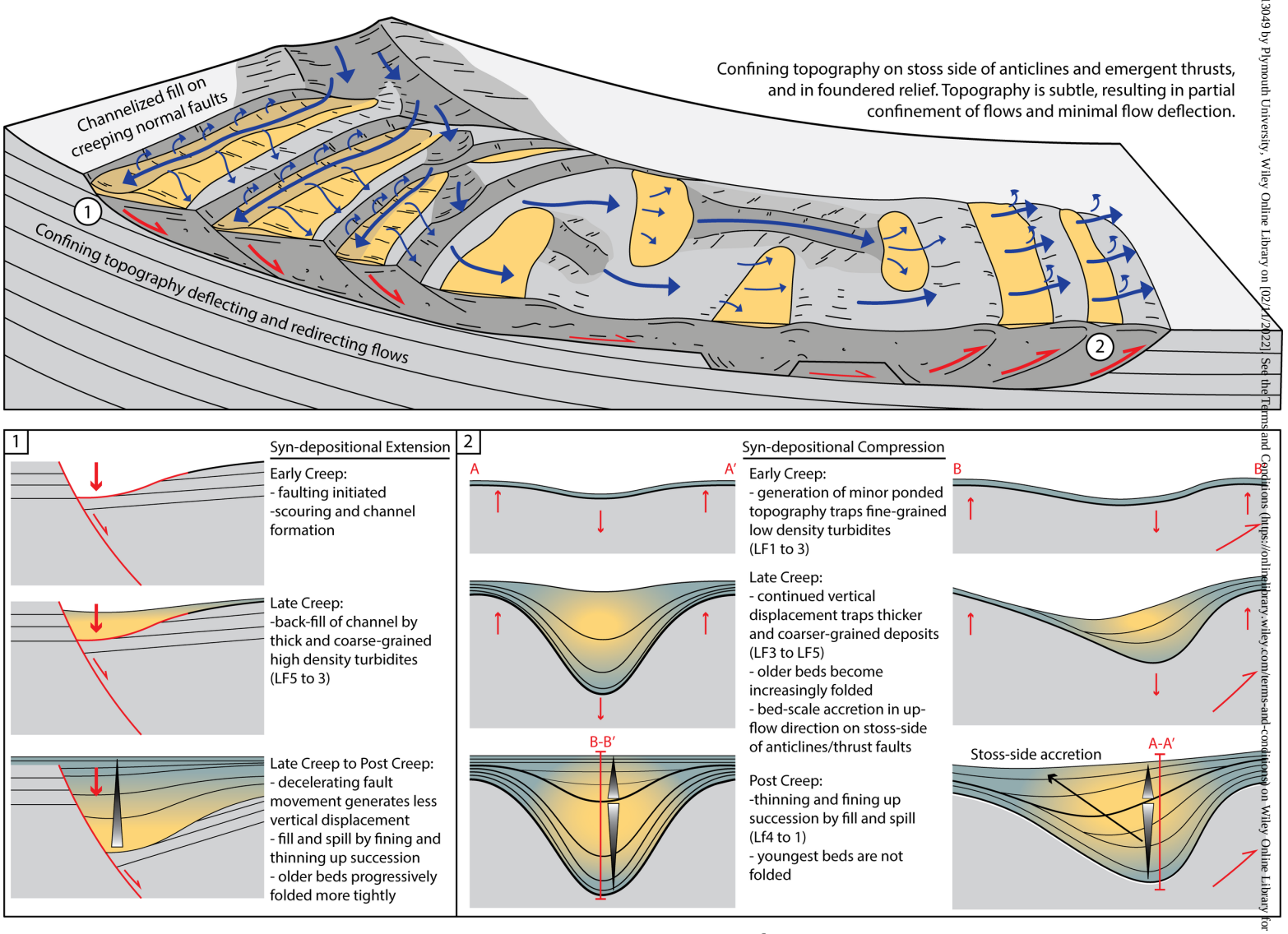

SED_13049_Fig. 11.tif

SUGGESTED FIGURE/TABLE SIZES FOR: SED-2021-OA-259.R2

FIGURES

	Single Column Width	2/3 Page Width	Full Portrait Page	Full Landscape Page
Figure 1*		x	x	
Figure 2			x	
Figure 3			x	
Figure 4			x	
Figure 5			x	
Figure 6	x			
Figure 7			x	
Figure 8	x			
Figure 9			x	
Figure 10			x	
Figure 11			x	

*between 2/3 and full page width

TABLES

	Portrait	Landscape	Notes
Table 1		x	